Brain Tumor Growth Simulation

Olivier Clatz, Pierre-Yves Bondiau, Hervé Delingette, Maxime Sermesant,
Simon K. Warfield, Grégoire Malandain, Nicholas Ayache

To cite this version:

Olivier Clatz, Pierre-Yves Bondiau, Hervé Delingette, Maxime Sermesant, Simon K. Warfield, et al.. Brain Tumor Growth Simulation. [Research Report] RR-5187, INRIA. 2004. inria-00071401

HAL Id: inria-00071401
https://inria.hal.science/inria-00071401v1

INSTITUT NATIONAL DE RECHERCHE EN INFORMATIQUE ET EN AUTOMATIQUE

Brain Tumor Growth Simulation

Olivier Clatz — Pierre-Yves Bondiau — Hervé Delingette — Maxime Sermesant —
Simon K. Warfield — Grégoire Malandain — Nicholas Ayache

N° 5187

Avril 2004

Thème BIO

Rapport
de recherche

ISSN 0249-6399

INRIA
SOPHIA ANTIPOLIS

Brain Tumor Growth Simulation

Olivier Clatz*, Pierre-Yves Bondiau†*, Hervé Delingette*,
Maxime Sermesant‡, Simon K. Warfield§, Grégoire Malandain*,
Nicholas Ayache*

Thème BIO — Systèmes biologiques
Projets Epidaure

Rapport de recherche n° 5187 — Avril 2004 — 45 pages

Abstract:

In the present report, we propose a new model to simulate the growth of glioblastomas multiforma (GBM), the most aggressive glial tumors. Because the GBM shows a preferential growth in the white fibers and have a distinct invasion speed with respect to the nature of the invaded tissue, we rely on an anatomical atlas to introduce this information into the model. This atlas includes a white fibers diffusion tensor information and the delineation of cerebral structures having a distinct response to the tumor aggression.

We use the finite element method (FEM) to simulate both the invasion of the GBM in the brain parenchyma and its mechanical interaction (mass effect) with the invaded structures. The former effect is modeled with either a reaction-diffusion or a Gompertz equation depending on the considered tissue, while the latter is based on a linear elastic brain constitutive equation. In addition, we propose a new coupling equation taking into account the mechanical influence of the tumor cells on the invaded tissues. This tumor growth model is assessed by comparing the *in-silico* GBM growth with the real GBM growth observed between two magnetic resonance images (MRIs) of a patient acquired with six months difference. The quality of the results shows the feasibility of modeling the complex behavior of brain tumors and will justify a further validation of this new conceptual approach.

Key-words: Tumor, model, glioblastoma, brain, Magnetic Resonance Imaging, growth, model, simulation, finite element, biomechanics, diffusion, infiltration, mass effect, Clinical Target Volume, Gross Tumor Volume.

---

* Epidaure Research Project, INRIA Sophia-Antipolis France
† Centre Antoine Lacassagne, Nice, France
‡ Computational Imaging Science Group, King's College, London. England
§ Computational Radiology Laboratory, Bigham and Womens Hospital, Boston, USA

Modélisation de la croissance de tumeurs cérébrales

Résumé : Nous proposons dans ce rapport une méthode permettant de simuler la croissance du glioblastome, la tumeur gliale la plus agressive. Cette simulation repose sur une modélisation couplée de deux effets : l'invasion par diffusion du glioblastome et la déformation mécanique des structures cérébrales voisines. Le premier phénomène est modélisé par une équation de type réaction-diffusion alors que le second repose sur les lois de comportement de la mécanique des milieux continus. L'équation de couplage permet de relier localement les efforts mécaniques à la densité de cellules tumorales dans le parenchyme cérébral.

Etant donné le caractère non homogène de la diffusion, nous utilisons un atlas anatomique cérébral dans lequel ont été segmentées les structures ayant un comportement spécifique vis-à-vis de la tumeur. En particulier, l'information issue de l'Imagerie par Résonance Magnétique de Diffusion (IRMd) permet de tenir compte de la tendance que présentent ces tumeurs à croître dans la direction des fibres de la matière blanche. Enfin, une première évaluation du modèle est effectuée en simulant la croissance d'un glioblastome chez un patient donné. Cette croissance *in-silico* est comparée à la croissance réellement obervée dans l'IRM du même patient 6 mois plus tard.

Mots-clés : tumeur, glioblastome, cerveau, imagerie par résonance magnétique, croissance, modèle, simulation, éléments finis, biomécanique, diffusion, infiltration, effet de masse.

Contents

1 Introduction

The majority of the primitive tumors of the central nervous system are from glial origin, among which the glioblastomas multiforma (GBM) are the most aggressive. Despite the substantial research effort against these pathologies, patients treated with state-of-the-art therapy have a median survival of approximately 1 year and six months.

Relatively little progress has been made toward the construction of a general model describing the growth of these tumors. The interest to carry out a simulation of the tumoral growth is multiple. First, it allows to get a better understanding of the physiology of tumor growth. Second, it could help to quantify the tumor aggressiveness of a given patient. Last, such a model could improve therapy planning (in surgery or radiotherapy) by better defining the invasion margins using the tumoral cell density estimation.

1.1 Understanding Tumor Physiology

A primary objective of our model is to investigate the 3D invasion of brain tumors and in particular the respective influence of tumor diffusion and mass effect. The work reported in this paper, including a case study, should be seen as a proof-of-concept towards this goal. Because our tumor growth model is based on MR imaging, we can relate the tumor invasion with anatomical and functional data of the brain.

For instance, a rapid invasion of a GBM through the corpus callosum may induce clinical symptoms related to a damaged brain area although the tumor cannot be detected on the MRI in this area.

1.2 Assessing the Tumor Rate of Growth

The invasion speed of some lesions can be more important than others, due to a greater "aggressiveness". From the time series of MR images of a patient, it is possible to picture the 3D invasion of GBM in the patient brain [Haney *et al.*, 2001]. Since tumors can exhibit different rates of growth, It is then possible to find the best model parameters -that best match the predicted with the observed invasion- to characterize local or global tumor agressiveness. In another words, aggressiveness can be considered as one of the hidden parameters of the model and could be estimated by solving the following inverse problem: given a time series of images, the hidden parameters can be estimated as the ones resulting in the most realistic simulation with respect to the data.

1.3 Therapy Planning

In radiotherapy treatments, the delineation of the Clinical Target Volume (CTV) has to take into account the presence of isolated malignant cells in the area surrounding the edema. Such malignant cells cannot be seen in a T2-weighted MR image. By estimating a tumoral cell density, our approach could help to assess the risk of finding isolated malignant cells outside the edema, and thus can help to delineate the CTV.

Furthermore, the segmentation of the Gross Tumor Volume 1 and 2 (GTV1 and GTV2, see section 2.3 for a short description of the GTV classification and [Kantor *et al.*, 2001] for further details) is performed on a MR image acquired before therapy. Because a significant delay may occur between the image acquisition and the radiotherapy treatment, our tumor model could predict the additional tumor invasion at the treatment time.

Once a patient with a GBM has been treated, the recurrence occurs in average one year later. Radionecrosis, which is a radiotherapy complication, has the same signal in MRI than the tumor recurrence, but their law of growth are different. Here again, a numerical model could be used to discriminate radionecrosis from tumor recurrence.

Finally, we believe that an *in silico* tumor growth model could be of great interest for neurosurgeons since they have to estimate the trade-off between risks and benefits of surgical procedures. Indeed, the combination of a functional atlas with the tumor simulation can lead to the prediction of future functional impairments upon the tumor invasion in the patient brain.

2 Previous Work and Contributions

2.1 Tumor Growth Models

In 1932, Mayneord [Mayneord, 1999] employed the term "law of growth" for a sarcoma of a rat. Data suggest that each tumor growth can be modelled with a specific equation which can be interpreted in terms of biophysics parameters. Without loss of generality, tumor growth models can be classified into two categories depending on their observation scale:

- Cellular and microscopic models. These models describe the cellular division speed. Basic models consider isolated cell behavior (exponential, Gompertz), while more complex ones take into account the interaction between the cells and their environment (cellular automata).
- Macroscopic models. These models describe the evolution of the local tumor cell density. Most of these models rely upon a reaction-diffusion equation to account for the tumor propagation.

2.1.1 Exponential

The first work on an exponentially growing population was performed by Reverend T.R. Malthus in 1798. Exponential growth is the simplest proliferation law, $N(t) = N(0)e^{kt}$. It describes the population density N(t) at any time t as a function of the initial population density N(0) and the constant growth rate k. The k value depends on the intrinsic aggressiveness of the tumor.

This function is suited for quantifying the growth of small tumors during a short time. The analysis of clinical data seems to show that this model best describes an average growth of human tumors, rather than individual tumor [Retsky *et al.*, 1990].

2.1.2 Gompertz

Malthus work was later modified, in particular by Gompertz (1825). Beyond a certain size, the exponential growth slows down gradually and may approach a Malthusian asymptotic limit. Indeed the growth, which is initially exponential, is later limited to an asymptotic rate and is called the growth of Gompertz. Tumors develop, in the Gompertzien mode, with a growth rate decreasing with tumoral growth.

The publications based on the kinetics of Gompertz refer to an article by Laird in 1969 [Laird, 1969] showing the validity of the kinetics of Gompertz for some tumors. Laird measured the growth of "19 examples of 12 different tumors from the rat, mouse, and rabbit" and concluded that this growth model seems to be a general biological characteristic of the growth of tumors. The “Gompertz Growth Law” has been used to describe the growth rate of a solid, avascular tumor at the population level and has had some success in clinical application [Lazareff *et al.*, 1999, Bajzer, 1999].

2.1.3 Cellular Automata

The Gompertz and exponential models can be considered as microscopic models of tumor growth, because the interactions between cells and tissues are not taken into account. The cellular automata model makes the link between the microscopic proliferation and the macroscopic diffusion model.

This approach differs from deterministic approaches because it computes each division and interaction at a cell scale to simulate the macroscopic behavior of the tumor growth. Cellular automata are used to simulate the early growth of the tumors and to examine their early vascularization and metabolism. Gompertz curves can be considered as a simple case of automata.

The models incorporate the normal cells, the tumoral cells, necrotic space or vacuum, and the micro-vessels. The cells and the micro-vessels affect the extracellular concentration which, in turn, affect back the evolution of each automaton [Patel *et al.*, 2001]. Other models take into account the development of the social behavior, expressed in the co-operative cellular movement [Bussemaker *et al.*, 1997][1].

2.1.4 Diffusive Models

On the one hand, the exponential and Gompertz cellular models represent a good approximation of the microscopic behavior of the GTV1 in the GBM, which is not greatly affected by the nature of the surrounding tissue. On the other hand, the macroscopic diffusive component of the GBM depends on the nature of the brain tissue. Recent attempts have been made to model this infiltrating component, taking into account local diffusivity parameters.

The diffusive models propose a macroscopic way of considering the tumor growth. Major contributions in this domain refer to the reaction-diffusion formalism proposed by Murray

---

[1] Some cellular automata are available on the Internet: `http://calliope.gs.washington.edu/software/otherSoftware.html`

in 1989 [Murray, 1989]:

$$\underbrace{\frac{\partial c}{\partial t}}_{\text{Tumor density evolution}} = - \underbrace{div\,(\underline{J})}_{\text{Diffusion law}} + \underbrace{S(c,t)}_{\text{Source factor}} - \underbrace{T(c,t)}_{\text{Treatment law}} \tag{1}$$

- c represents the tumor cell density.
- $\underline{J}$ represents the diffusion flux of tumoral cell [2], which flux obeys the Fick's law, i.e. the diffusion flux of cell is proportional to the gradient of tumor cell density:

  $$\underline{J} = -D\,\underline{\nabla c} \tag{2}$$

  D is the diffusion coefficient.
- $S(c,t)$ represents the source factor function.
- $T(c,t)$ is used to model the efficacy of the tumor treatment.

This diffusion equation proposed by Murray [Murray, 1989] is the basis of the major work in diffusive tumor models [Chaplain, 1996, Swanson *et al.*, 2002]. Later models [Tracqui, 1995] include the mechano-chemical aspect of cell mobility by including an active cell mobility term in the reaction-diffusion equation.

2.2 GBM Tumor Growth

2.2.1 Cellular Tumor Growth

Tumor growth results from tumor cell division. After each cell division cycle, the cell population doubles so as to increase by a factor 2^N after N cycles.

This equation would be valid if each cell could duplicate itself in each cycle and if there were no cellular loss. However, during the tumor growth, blood flow decreases and there is a lack of oxygen and nutriments, causing cellular death by necrosis. This loss is responsible for the slowing of the kinetics of tumoral growth and can be expressed as a fraction of loss per unit of time.

Therefore, tumor growth results from an imbalance between cell birth and cell death. The limitation of human experimentation explains the relatively sparse data available on the evolution of tumors. Moreover, malignant tumors consist of different cellular populations, each with different properties and behaviors [Kansal *et al.*, 2000]. Tumoral growth is often unpredictable.

---

[2] Except when using homogeneous coordinates, "$\underline{\ }$" represents a 3×1 vector and "$\underline{\underline{\ }}$" a 3×3 matrix.

2.2.2 Classification And Mortality

Glioblastomas can be classified as primary or secondary. Primary GBMs represent the majority of cases (60%) more often in older patient (> 50years) while secondary GBMs typically develop in younger patients (< 45years) through malignant progression from a low-grade astrocytoma. This progression shows a large variability, from 1 to 10 years. Whereas both are classified as glioblastomas, there is increasing evidence that primary and secondary GBMs evolve as distinct diseases.

Despite the substantial research effort towards improving tumor treatment, no significant advances in the treatment of glioblastomas have occurred in the past 25 years. Without therapy, patients with GBMs usually die within 10 months. Patients treated with state-of-the-art therapy, including surgical resection, radiation therapy, and chemotherapy, have a median survival of approximately 1.5 years. There is as yet no evidence that patients with a secondary GBM have a better prognosis than patients with a primary GBM.

2.2.3 Glioblastoma Models

Previous publications focusing on modeling glioblastomas isolate two key characteristics: a proliferation component and a diffusion component [Tracqui, 1995] [Swanson *et al.*, 2002] [Burgess *et al.*, 1997] [Tracqui *et al.*, 1995]. These two characteristics can be related to the categories described in section 2.1: the proliferation component often corresponds to the central active part of the tumor and can be described with a cellular proliferation law; the diffusion component is generally associated to the external part of the tumor and can be described by a diffusion law. Glioblastoma mutiforma can thus be described as a combination of two different growth models depending on the considered tumor area (central active or external).

2.3 Contributions

In this report, we propose a patient-specific simulator of glioblastoma growth, including the brain deformation (mass effect) induced by the tumor invasion. The simulation relies upon a Finite Element Model (FEM) initialized from the patient MRIs. Additional information has been included in the patient model using an atlas to take into account the behavior of the different structures with respect to the tumor invasion, such as the white matter fiber directions.

Furthermore, we propose to make the link between the radiotherapy classification of tumors in Gross Tumor Volumes (GTV) proposed in some protocols for radiotherapy treatment [Kantor *et al.*, 2001] and the two distinct invasion behavior:

- The GTV1 is associated with the expansion component. Because it does not infiltrate the tissue, this proliferation is directly correlated with a volume increase. By creating new cells, the GTV1 pushes away its surrounding structures. It is therefore responsible for the major mechanical mass effect on the brain. For instance, the GTV1 is described in our model by an exponential law describing this volume increase.

- The GTV2 is associated with the diffusion component. It invades adjacent structures by a diffusion process and is responsible for the infiltration in white and gray matter. This diffusion component expands faster than the GTV1 but exhibit a smaller mass-effect. The GTV2 is thus described in our model with a reaction-diffusion equation. In addition, we propose to model its associated mass effect with a coupling equation which links the mechanical to the diffusion process.

An example of the usual GTV segmentation can be seen on figure 1. The model is initialized on a standard segmented patient MRI. The goal is to simulate the growth process of the GBM with the help of an atlas, starting with this early MRI and to compare its expansion with the MRI of the patient at a later stage.

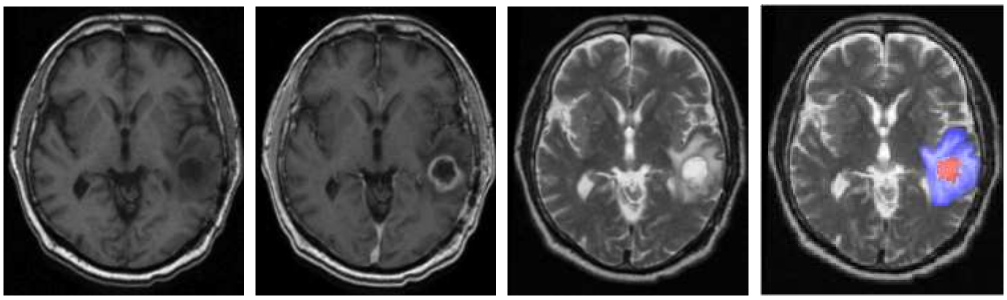
(a) (b) (c) (d)

Figure 1: MR images of a patient (a) T1; (b) T1 with gadolinium injection; (c) T2; (d) GTV1 (red) and GTV2 (blue) segmentations overlaid on the T2 MRI.

Compared to the previous publications dealing with the tumor growth modeling problem ([Swanson *et al.*, 2002] [Tracqui and Mendjeli, 1999] [Chaplain, 1996]), our approach includes several improvements:

- A full 3D model, instead of a 2D one, for both diffusion and deformations is used. The mechanical and diffusion parameters are initialized based on a volumetric segmented atlas.
- The use of diffusion tensor imaging to take into account the anisotropic diffusion process in white fibers (as opposed to the isotropic reaction-diffusion formalism of Murray [Murray, 1989, Swanson *et al.*, 2002]).
- The use of the radiotherapy volume classifications to initialize the source of the diffusion component (as opposed to point sources in [Swanson *et al.*, 2002]).
- A new coupling equation between the reaction-diffusion and the mechanical constitutive equation to simulate the mass-effect during of the VG growth.

- The initialization with a patient tumor and a quantitative comparison with the observed invasion in the later patient MR images.

3 Glioblastoma Growth Simulation

3.1 Overview of the Method

Our GBM growth simulation consists of two coupled models :

1. A model for the diffusion of the tumor that captures the evolution of the tumor density c over time.
2. A model for the expansion of the tumor that predicts the mass effect induced by the tumor proliferation.

The coupling between these two models is further described in section 3.4.3 but it assumes the following behavior: the mass effect is directly related to the tumor density c but the tumor density c is not influenced by the mass effect.

This simple coupling leads to a four step algorithm described in Figure 2 :

- **Image segmentation and registration.** The two gross volumes - GTV1 and GTV2 - are manually delineated by an expert (who regularly segments these tumors in MR images for clinical radiotherapy treatments) from the patient MR images. The patient MR images are registered with respect to an anatomical atlas. This atlas includes for each voxel the location of the main cerebral structures and a diffusion tensor in the white matter.
- **Meshing and Initialization.** A tetrahedral mesh of the patient's brain is built in the atlas reference frame. Tissue properties are assigned to their associated tetrahedra using the atlas. Furthermore, the value of the tumor density c is initialized based on the GTV1 and GTV2 segmentations by interpolating between the two boundaries.
- **Simulation.** The simulation of the VG (Virtual Glioblastoma) diffusion and expansion is performed on the finite element mesh following the mechanical and diffusion equations.
- **Comparison.** At the end of the growth process, new GTV1, GTV2 and local deformations of the atlas are registered to the patient images. Then, an assessment of the relevance of the model is performed by comparing the predicted tumor volumes with the ones observed from patient MR image acquired six months later.

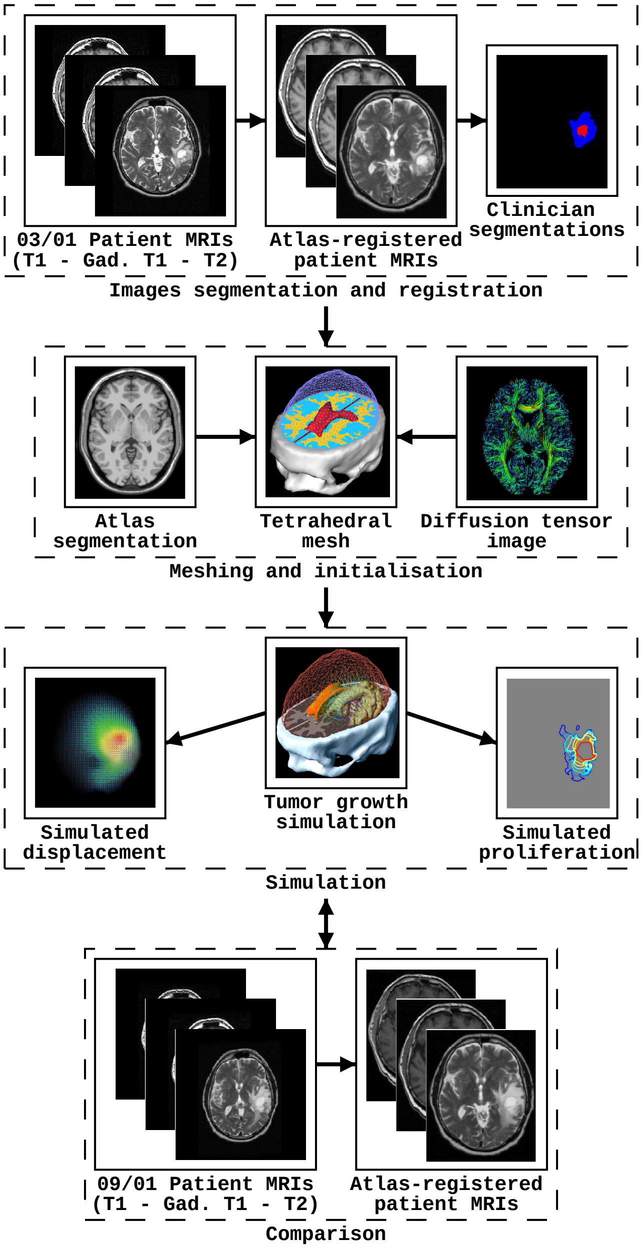

Figure 2: Flowchart of the proposed approach

3.2 Pre-Processing of MR Images

3.2.1 Patient

Standard imaging protocols for brain tumor radiotherapy have been used for this study. Three sequences, T1, T2, and T1 with gadolinium injection (exported in Dicom-3 format) were used for this study; and two different series of MRIs of the same patient were acquired with 6 months difference (Figures 3 and 4). The size and format of the images are shown in Table 1. These MRIs have been acquired in the standard follow-up, after surgical resection, radiotherapy treatment and/or chemotherapy [Frenay *et al.*, 2000]. No treatments were started for the recurrent GBM before clinical symptoms.

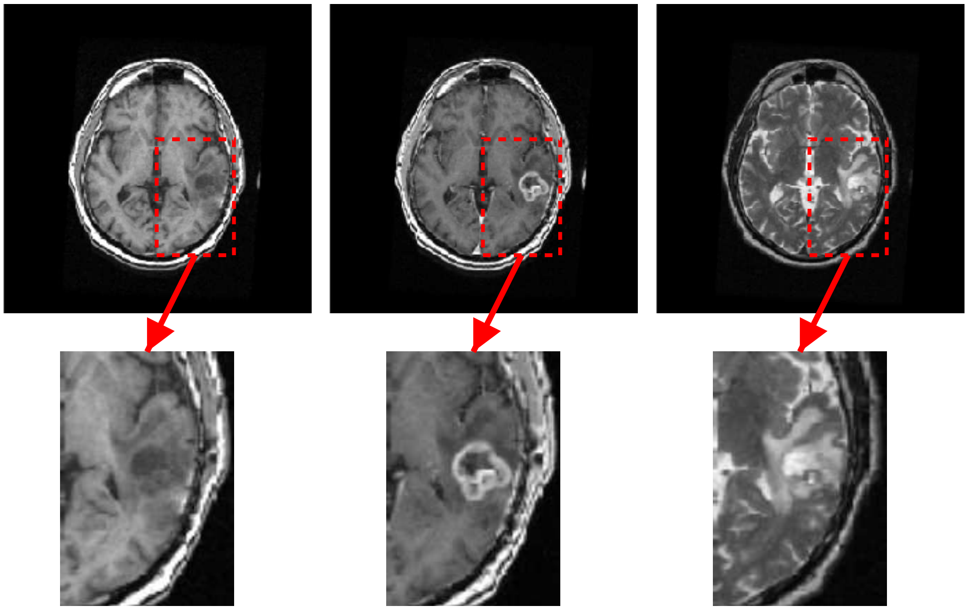
T1 T1+ gadolinium injection T2

Figure 3: First MRI series (T1 - T1 + gadolinium injection - T2), acquired in March 2001.

3.2.2 Tumor Segmentation

The initial tumor location is used to set the boundary conditions of our finite element model. This was performed manually by a medical expert using the three acquisition modalities. Because the external ring of the Gross Tumor Volume (GTV1) represents the most active part of the tumor, it is enhanced by gadolinium. Its boundary is therefore defined as the area

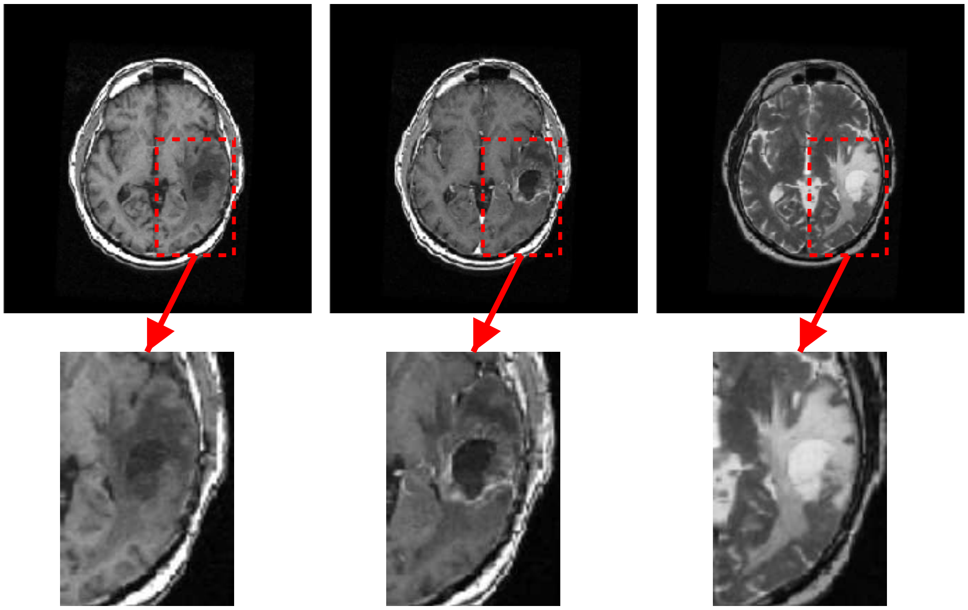

T1 T1+ gadolinium injection T2

Figure 4: Second MRI series (T1 - T1 + gadolinium injection - T2), acquired in September 2001.

	Image size	Voxel size (mm)
MRI T1	256*256*60	1.015*1.015*2
MRI T2	256*256*64	1.015*1.015*1.9
Virtual MRI T1	181*217*181	0.6*0.6*0.6
Virtual MRI T2	181*217*181	0.6*0.6*0.6
DTI	256*256*36	1.0*1.0*4.0

Table 1: MRIs characteristics

of contrast enhancement observed on the T1-weighted MRI following gadolinium injection. The GTV2 takes into account the probability of presence of isolated malignant cells in the edema surrounding the tumor. Its boundary is therefore delimited by the area of hyper-signal in the T2-weighted MRI, as proposed in the protocols for radiotherapy treatment.

3.2.3 Registration

The following affine registrations are computed using the Baladin [Ourselin *et al.*, 2000] software. This algorithm computes the transformation in three steps in a coarse to fine approach:

- Estimate the displacements $\underline{d}\left(\underline{X_i}\right)$ of a domain V composed of voxels centered in $\underline{X_i}$ ($\underline{X_i} \in V$ starting with the full image) from the reference image to the target image based on a block matching approach. In our case, we use the sum of squared differences as a similarity measure, since both images are the same image modality.
- Find the optimal affine transformation $\underline{T}\left(\underline{X}\right) = \underline{\underline{F}}\,\underline{X} + \underline{C}$ that minimizes the transformation error with respect to the measured displacements $\underline{d}(\underline{X_i})$:

$$\underline{T} = \arg\min_{T} \left(\sum_{\underline{X_i} \in V} \left\| \underline{T}(\underline{X_i}) - \underline{d}(\underline{X_i}) \right\|^2 \right) \tag{3}$$

- Discard the outliers from the voxels in the domain V using a least trimmed square estimator [Rousseeuw, 1984].

To obtain a better matching between deep brain structures, we remove the skull from both images and compute the affine transformations on brains only.

3.2.4 Building an Atlas

An atlas usually consists in an anatomical MR image and an associated label for each voxel representing the nature of the tissue. In our case, we propose to add a diffusion tensor information to the white fiber labeled voxels.

This atlas was built from two images, a labeled MR image used as an anatomical atlas, and a diffusion tensor image registered with the anatomical MRI.

Anatomical Atlas We used a fully artificial MRI for the anatomical atlas, generated by the "brainweb" software [Cocosco *et al.*, 1997]. The structures delineation is then performed with different thresholds on this MRI. However an assymmetry exists and can introduce a bias. Thus we mirrored the right part of the head to generate a perfectly symmetrical atlas MRI (see Figure 5). Artificial MRI characteristics are shown in Table 1. To minimize partial volume effect when matching, a high definition MRI with smaller voxels than the patient MRIs was used. We focused on different structures of interest for the purpose of tumor growth simulation: skull, ventricular system, brain (gray matter and white matter) and falx cerebri (see figure 5) according to the anatomical data of the atlas of Talairach [Talairach and Tournoux, 1988]. This atlas is used to initialize the patient finite element model.

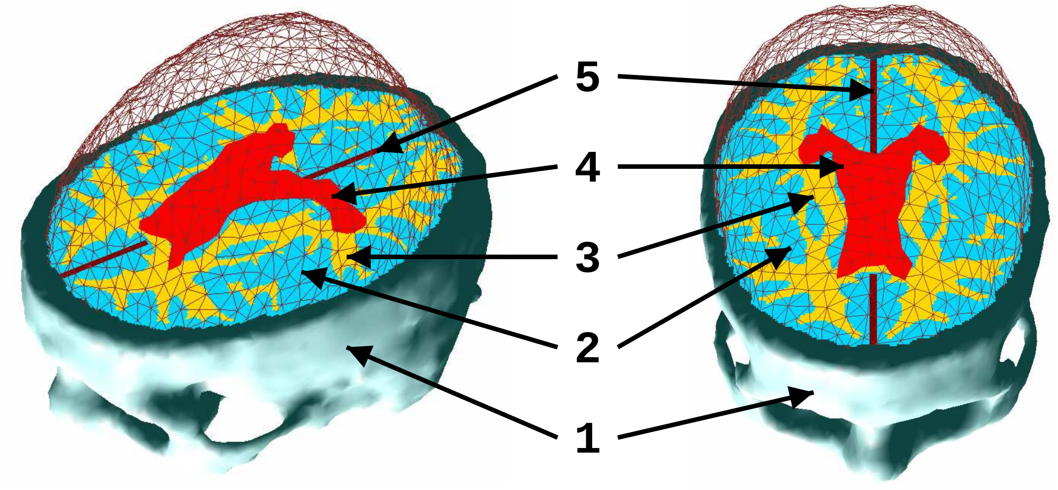

Figure 5: The brain atlas mesh used to generate the tetrahedral mesh: (1) the skull, (2) gray matter, (3) white matter, (4) ventricles, (5) falx cerebri.

Diffusion Tensor Information The GBM is a tumor of glial origin and grows preferentially in the white fiber directions [Price *et al.*, 2003]. To take these fact into account and to be more accurate in both direction and speed of progression of the tumor, data from Diffusion Tensor Imaging (DTI) was used in the white matter.

The DTI measures the variance of the conditional probability $P(\underline{X}|\underline{X_0}, t)$, which represents the probability of finding a water molecule at a position $\underline{X}$ and at time t given its original position $\underline{X_0}$:

$$\left\langle \left(\underline{X} - \underline{X_0}\right) \cdot \left(\underline{X} - \underline{X_0}\right)^T \right\rangle = 6\, \underline{\underline{D}}\, t \tag{4}$$

Where $\langle Y \rangle$ stands for Expectation(Y).

This DTI is reconstructed from n diffusion gradient images ($n \geq 6$) and a null gradient image (T2 weighted). This diffusion is about $2.9 * 10^{-3}\ mm^2\ s^{-1}$ in pure water and three times larger in the fibers direction ($1.2 * 10^{-3}\ mm^2\ s^{-1}$) than in the transverse direction $0.4 * 10^{-3}\ mm^2\ s^{-1}$.

Using notations defined in section 3.2.3 for the affine transformation, the registered diffusion tensor image $\underline{\underline{D'}}$ is mathematically defined as:

$$\underline{\underline{D'}}(\underline{X_0}) = \underline{\underline{F}}\ \left[\underline{\underline{D}}(\underline{\underline{F}}^{-1}(\underline{X_0} - \underline{C}))\right] \underline{\underline{F}}^T \tag{5}$$

We decompose this tensor registration in three steps:

- Finding the affine transformation T which displaces a voxel at position $\underline{X}$ to the position $\underline{X'} = \underline{T}(\underline{X}) = \underline{\underline{F}}\,\underline{X} + \underline{C}$ in the atlas MRI. This registration is performed using the T2 weighted MRI in the original DTI data set.

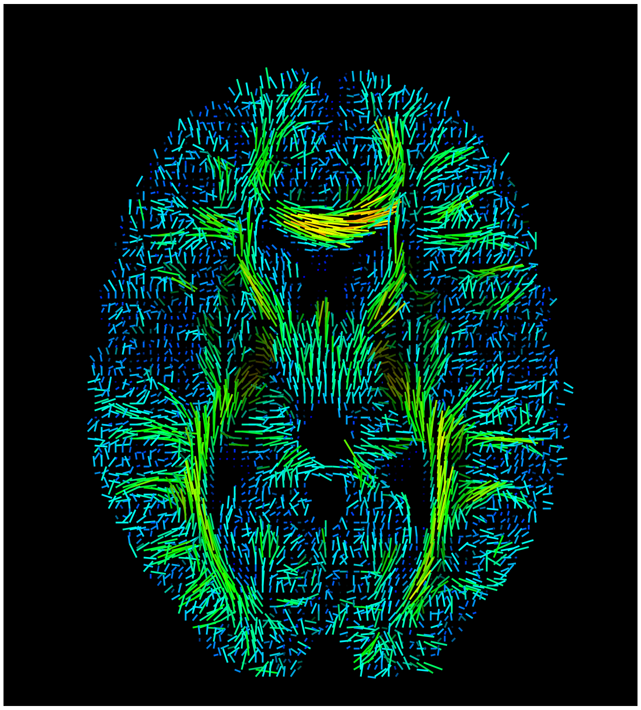

Figure 6: Axial slice of the registered DTI

- Compute $\underline{\underline{D}}^* = \underline{\underline{D}}(\underline{\underline{F}}^{-1}(\underline{X_0} - \underline{C}))$ which corresponds to registering each gradient image in the atlas geometry.
- Compute $\underline{\underline{D}}'(\underline{X_0}) = \underline{\underline{F}}\,\underline{\underline{D}}^*\,\underline{\underline{F}}^T$.

Since we compute our transformation $\underline{T}$ in voxel coordinates, we re-sample every DT image after the second step with a voxel size equal to the atlas size, to remove the scaling effect due to the difference in voxel sizes. In addition, we require that the affine registration process does not change the underlying tissue absolute diffusivity properties. As proposed in [Sierra, 2001], we remove the scaling factor $(det(\underline{\underline{F}})^{\frac{2}{3}})$ from the transformation to obtain the final diffusivity tensor image. Figure 6 shows an axial slice of the registered diffusion image.

3.3 Diffusion Model

3.3.1 Diffusion Equation

We rely on the reaction-diffusion model (equation 1) to account for the growth and the spreading of tumor cells in the brain parenchyma. Since the purpose is only to simulate the tumor growth, we will not consider the treatment term $T(c,t)$ for this model. In addition we propose to model the anisotropy of malignant cell diffusion in the white matter considering a diffusion tensor $\underline{\underline{D}}$:

$$\underline{J} = -\underline{\underline{D}}\,\underline{\nabla c} \tag{6}$$

$\underline{\underline{D}}$ represents the local diffusivity of the tissue and depends on the white fibers direction and the nature of the tissue. To minimize the number of tumor-intrinsic parameters, we use a simple linear function to model the source factor, reflecting its aggressiveness:

$$S(c,t) = \rho c \tag{7}$$

Then combining equations 7 and 6 with 1, we can express the diffusion law:

$$\frac{\partial c}{\partial t} = div\left(\underline{\underline{D}}\,\underline{\nabla c}\right) + \rho\, c \tag{8}$$

In this equation, c represents the normalized cell density ($c \in [0,1]$). The real cell density C is obtained by multiplying c with the carrying capacity of the tissue C_{max} estimated to be equal to $3.5 \times 10^4\, Cells\, mm^{-3}$ [Cruywagen *et al.*, 1995, Tracqui *et al.*, 1995].

The local behavior of the tumor therefore only depends on the diffusion tensor $\underline{\underline{D}}$ and the source factor ρ.

To better understand the role of anisotropy in the diffusion process, we solved equation 8 on two test-cubes (see figure 7), initializing a random shape tumor centered in the cube and varying the anisotropy of $\underline{\underline{D}}$:

$$\underline{\underline{D_{iso}}} = D_0 \begin{bmatrix} 1 & 0 & 0 \\ 0 & 1 & 0 \\ 0 & 0 & 1 \end{bmatrix} \text{ and } \underline{\underline{D_{aniso}}} = D_0 \begin{bmatrix} \mu & 0 & 0 \\ 0 & 1 & 0 \\ 0 & 0 & \mu \end{bmatrix} \text{ with } 1 > \mu > 0.$$

3.3.2 Model Parameters and Initialization

Because the diffusion process does not occur in the skull or in the ventricles, we mesh only the brain. We will see later that this mesh is also compatible with mechanical boundary conditions. Then, we propose the following characteristics for the model:

- Since the conductivity of the skull and the ventricles is null, the flux at the mesh surface should be zero. Therefore the boundary condition for the mesh surface is:

$$\underline{J} \cdot \vec{n} \;=\; 0$$

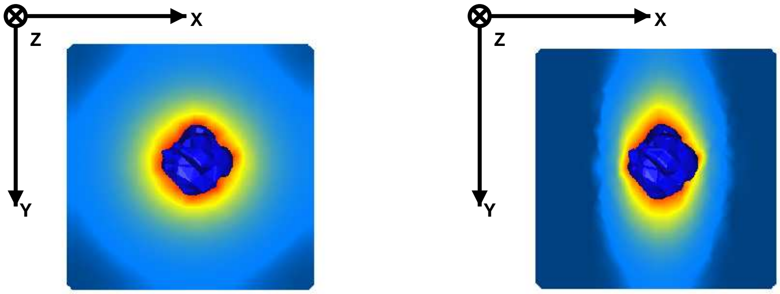

Figure 7: Behavior of the diffusion equation on test cases: isotropic (left) and anisotropic: $\mu = 0.1$ (right).

Tissue	diffusivity $(10^{-3}\, mm^2\, s^{-1})$
White matter	$\alpha \cdot$ DTI (anisotropic)
Gray matter	$\beta \cdot max(\underline{\underline{D}}_{White})$ (isotropic)
Ventricles	0 (isotropic)
Skull	0 (isotropic)
Falx cerebri	0 (isotropic)

Table 2: Diffusivity property of the atlas segmented tissues

- We use the previously described diffusion atlas (see section 3.2.4) to initialize the diffusion tensor $\underline{\underline{D}}$ in white matter. The intrinsic aggressiveness of the tumor is then controlled by two parameters α and β.

- There are several indications that glioblastomas diffuse more slowly in the gray matter than in the white matter [Swanson *et al.*, 2000]. Thus diffusivity in gray matter is chosen as a fraction of the maximum diffusivity in white matter $\beta = \frac{D_{white}}{D_{gray}}$. We choose a constant isotropic diffusion tensor and the ratio coefficient $\beta = \frac{1}{100}$, which visually best simulate the *in-silico* diffusion of the GBM in gray matter for our patient.

- Because tumor cells cannot diffuse through the falx cerebri, we set its diffusivity to zero.

- The GTV1 capacity is set to the maximum carrying capacity of the brain tissue C_{max} $(3.5 \times 10^4\, Cells\, mm^{-3})$.

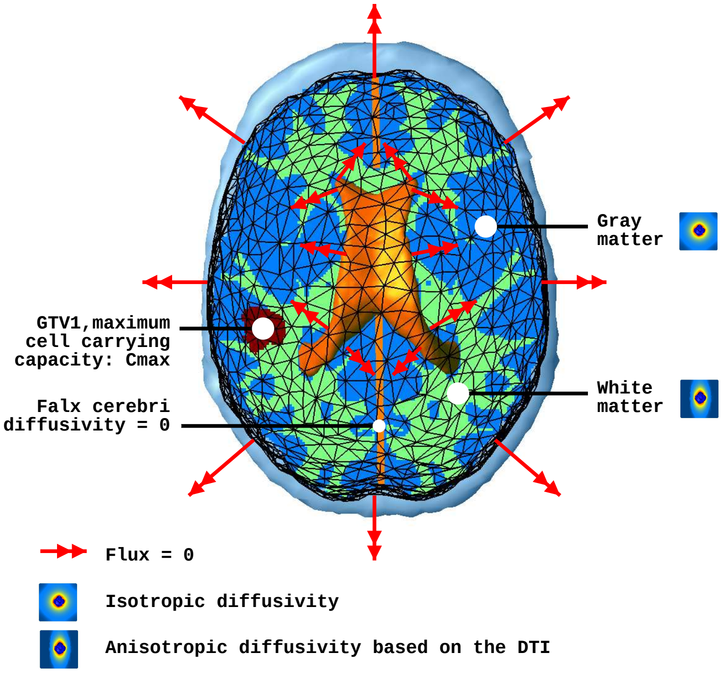

Figure 8: Diffusion model and boundary conditions summary.

- As discussed in [Swanson *et al.*, 2003], one cannot determine both α and ρ from only two different instants. We thus arbitrarily set $\rho = \frac{\eta}{100}$ (η is defined in section 3.4.2). The α parameter is then adapted to the GTV2 diffusion speed.

The material diffusivity values are summed up in Table 2. Figure 8 summarizes the diffusion model and the boundary conditions. We use the model to solve the stationary version of equation 8, so as to interpolate the c function between the two initial contours delineating the GTV1 and GTV2 (Figure 9).

3.4 Mechanical Model

3.4.1 Brain Constitutive Equation

One can find in the literature several rheological experiments performed on the brain tissue. Most relevant ones in this domain are certainly those conducted by Karol Miller [Miller, 2002] and Michael Miga [Miga *et al.*, 2000]. In particular, Miller has been involved into several in-vivo experiments on pig brains. He proposes that brain tissue can be modeled with an homogeneous hyper-viscoelastic non-isotropic material. However, he insists on the fact that

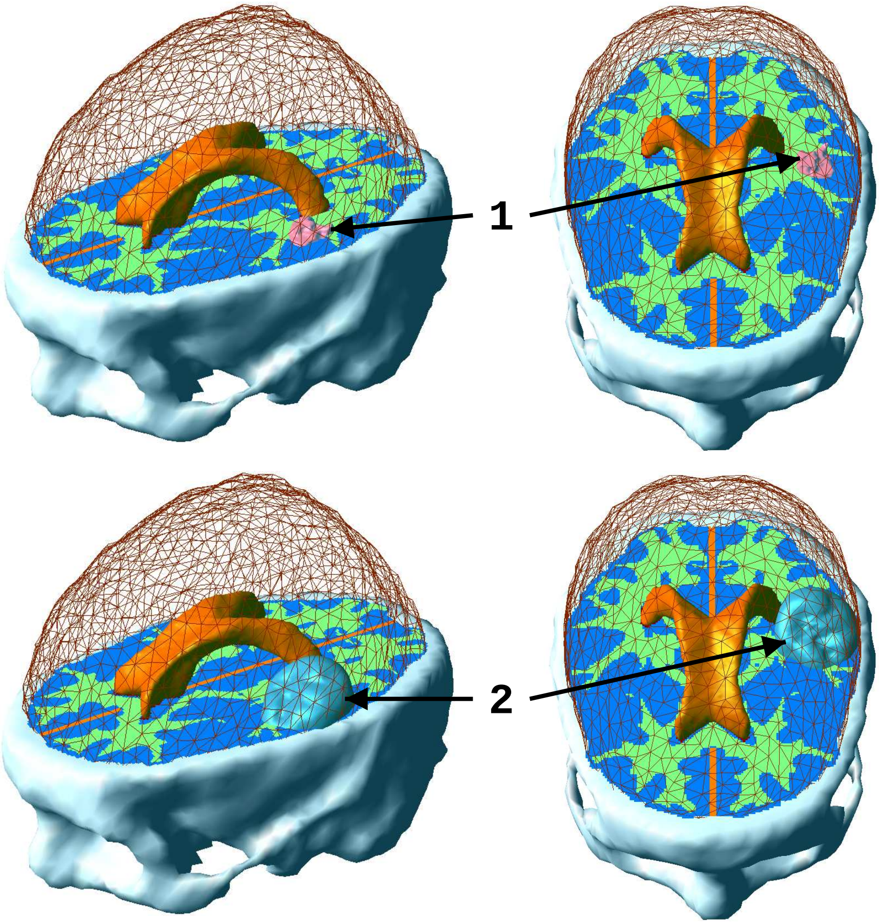

Figure 9: Tumor initialisation in the finite element model. 1. GTV1, 2. GTV2

further research still need to be done, and especially to estimate the influence of friction between the brain and the skull.

3.4.2 Mechanical Equation

We use the classical continuum mechanics formalism [Fung, 1993] to describe the mechanical behavior of the brain parenchyma. Since the deformation is very slow, we propose to use the static equilibrium equation:

$$div\left(\underline{\underline{\sigma}}\right) + \underline{f_{ext}} = 0 \tag{9}$$

with $\underline{\underline{\sigma}}$ the internal stress tensor (Pa) and $\underline{f_{ext}}$ the external force applied on the model (N).

Although brain tissue is nonlinear and viscoelastic, Miller's experiments ([Miller, 2002]) proposed that for very slow deformations ($<< 50\,sec$), the 1D stress/strain non-linear constitutive equation of the brain parenchyma can be written as:

$$\sigma = \frac{2}{\gamma^5}\left(1 - g_1 - g_2\right)\left(-1 - \gamma + \gamma^3 + \gamma^4\right)\left(\left(2C_{200}\right)\left(1 - \gamma - \gamma^3 + \gamma^4\right) + C_{100}\gamma^2\right)$$

with:

- γ is related to the strain ϵ: $\epsilon = ln(\gamma)$.
- σ is the uniaxial stress.
- $g_1 = 0.450,\ \ g_2 = 0.365$
- $C_{100} = 263\,Pa$, $C_{200} = 491\,Pa$

Since the growing process is very slow in our case ($>> 1day$), and the measured deformation in the parenchyma is in the small deformation range ($\leq 5\%$), we propose to linearize this equation. We thus consider linear relationship for both the constitutive equation and the strain computation:

$$\underline{\underline{\sigma}} = \underline{\underline{K}}\,\underline{\underline{\epsilon}} \tag{10}$$

$$\underline{\underline{\epsilon}} = \frac{1}{2}\left(\underline{\underline{\nabla u}} + \underline{\underline{\nabla u}}^T\right) \tag{11}$$

- $\underline{\underline{K}}$ is the rigidity matrix (Pa).
- $\underline{\underline{\epsilon}}$ is the linearized Lagrange strain tensor expressed as a function of the displacement $\underline{u}$ (no units).

By minimizing the squared stress error committed with the linear elasticity approximation in the range of small compressions ($\epsilon \in [-0.1\,;\,0.0\,]$), we found an optimal Young modulus $E = 694\,Pa$. We computed that the absolute error in the stress with this choice is below $4.2\,Pa$ (see Figure 10).

3.4.3 Mass Effect

We propose to make the difference between the mass effect related to the GTV1 volume expansion and the one related to the diffusion of tumoral cells into the rest of the brain. We thus consider two distinct equations describing the mass effect depending on the considered brain area position with respect to the GTV1.

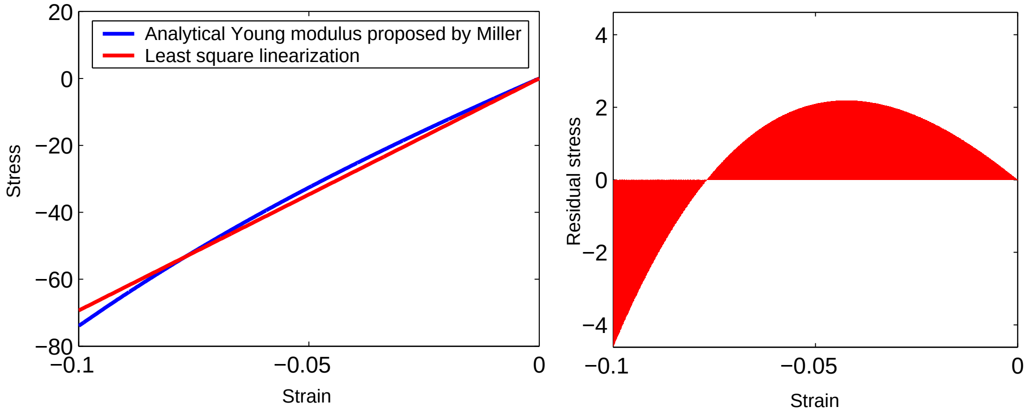

Figure 10: (Left) constitutive equation proposed by Miller and linear approximation; (right) error in stress with the linear approximation.

Inside the GTV1 Because the GTV1 is modeled as a pure cell proliferation and since the associated tissue is already considered saturated with tumoral cells, this proliferation directly acts as a volume increase on the GTV1. This volume increase ΔV can be computed at time t:

$$\Delta V = V_t - V_0 = V_0 \left(e^{\eta t} - 1 \right)$$

Based on the proposed model, η can be approximated by computing the average volume increase of GTV1 in GBM. We found $\eta = 2.2 \times 10^{-3} day^{-1}$. However, because of the GTV1 inhomogeneity and because cells can be exchanged between the GTV1 and the GTV2, η does not directly characterize the GTV1 cells aggressiveness but represents an average volume expansion speed. As proposed in [Kyriacou and Davatzikos, 2001] we use a penalty method to impose this volume variation boundary condition via a homogeneous pressure into the GTV1.

Outside the GTV1 Wasserman proposed in [Wasserman and Acharya, 1996] modeling the mechanical expansion of the tumor volume by a pressure P proportional to N/V, with N the total tumor cell count and V the total volume of the tumor. We propose a new equilibrium equation to model the mechanical impact of the tumor on the invaded structures.

$$div \left(\underline{\underline{\sigma}} - \lambda \, \underline{\underline{\mathbb{I}_3}} \, c \right) + \underline{f_{ext}} = 0 \tag{12}$$

This equation is the differential version of the law proposed in Wasserman's paper. The effect of this coupling equation can be seen on Figure 11. It can be locally interpreted as a tissue internal pressure proportional to the tumor concentration.

We use the previous law to describe the mechanical effects of the malignant cells invading the brain parenchyma.

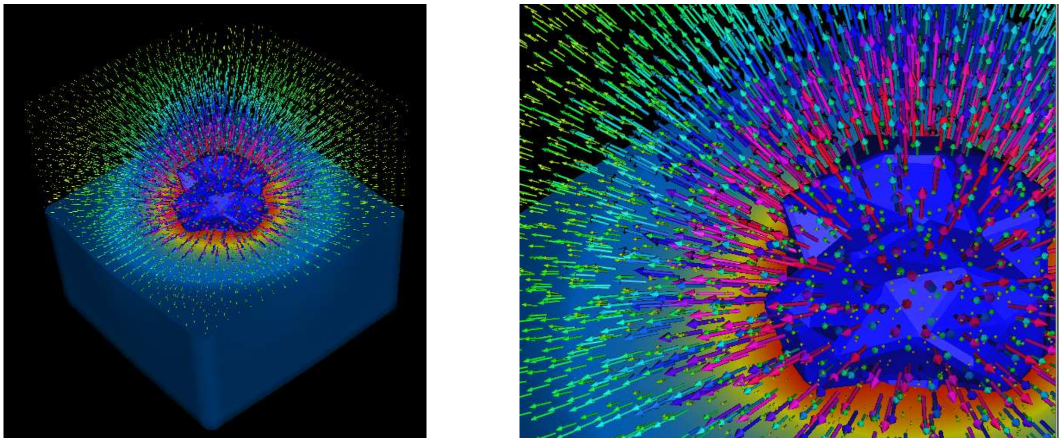

Figure 11: Influence of the coupling equation 12 on the mechanical behavior of the brain parenchyma using an isotropic diffusion test-case.

Tissue	Young Modulus (Pa)	Poisson Coefficient
White	694	0.4
Gray Matter	694	0.4
Falx Cerebri	200,000	0.4
Ventricles	0	0
Skull	∞	0.5

Table 3: Stiffness properties of the atlas segmented tissues or equivalent boundary conditions

3.4.4 Model Parameters And Initialization

The proposed mechanical model is similar to the one used for predicting intra-operative deformations [Clatz *et al.*, 2003]. It has following characteristics:

- The skull does not deform and is considered infinitely rigid. Thus vertices on the surface of the brain mesh are fixed.
- We use the linearized 3D homogeneous version of Miller's constitutive equation (see 3.4 for details), the Young modulus is set to $694\,Pa$. One could also consider the additional anisotropy due to the white fibers. However without significant rheological experiments on this subject, we consider the brain tissue to be isotropic. We propose to model the brain parenchyma as almost incompressible, the Poisson coefficient is thus set to 0.40.

- Based on the intra-cranial flow model of Stevens [Stevens, 2000], considering that the cerebro-spinal fluid production is not affected by the tumor growth, and because the growth process is very slow, we can consider that the ventricular pressure is not affected by the tumor growth. Therefore we let ventricular vertices free without additional internal pressure.
- The falx cerebri is a stiff fold of the dura-mater in the mid-sagittal plane and sustains part of the hemispheres internal pressure. We propose to stiffen the part of the mesh consisting of the falx. Based on the experimental results [Schill *et al.*, 1996], we chose its Young modulus equal to $2 \times 10^5 Pa$.
- We choose a coupling factor λ which minimizes the quantitative difference between the model and the real deformations: $\lambda = 1.4 \times 10^{-9}\, N\, mm\, Cells^{-1}$. It corresponds to a 15% volume increase for a tissue with a saturated tumoral cell density C_{max}.

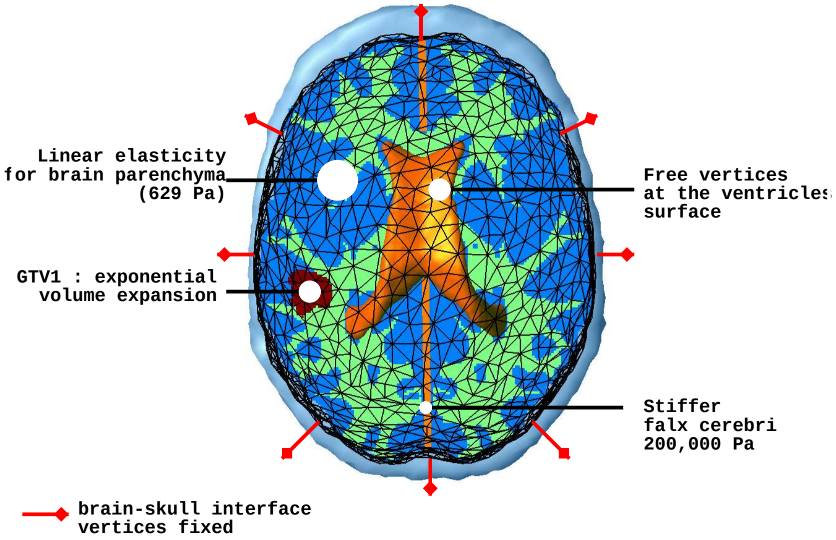

Figure 12: Mechanical model and boundary conditions summary.

The material mechanical properties are summarized in Table 3. Figure 12 shows the diffusion model and the boundary conditions.

3.5 Finite Element Modeling

We use the finite element method to solve the problem. This technique suited for solving problems described by a partial differential equation (PDE) consists in looking for solutions in a sub-vectorial space of finite dimension. The solution is thus expressed in the discretized domain by the shape functions and its associated nodal unknowns (more details about the general finite element framework can be found in [Bathe, 1982]). The details of both the method A and the numerical schemes B are given in appendix.

4 Results

4.1 Simulation Results

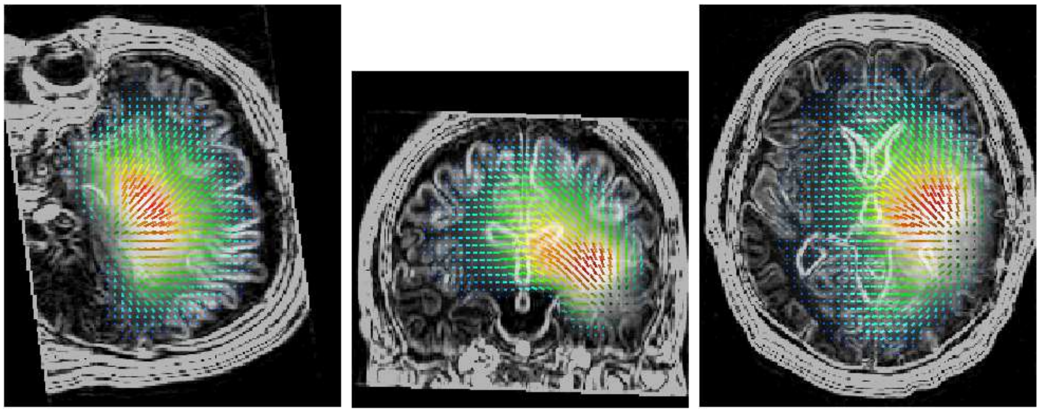

Figure 13: Displacement of the tissues induced by the tumor mass effect

After performing the simulation, we registered both the deformations and the tumor concentration into the first patient MRI (03/2001). Results are presented in two parts, the mass effect and the tumor diffusion.

4.1.1 Mass Effect

Figure 13 shows the displacement of internal tissue due to the mass effect. Even if these major displacements take place close to the GTV1, distant tissues in the same hemisphere are also affected by the tumor growth. The average displacement at the GTV1-GTV2 boundary is about 3 mm. Figure 15 shows an enlargement of structures directly affected by this mass effect. We can see that the tumor also pushes the mid-sagittal plane away. The tumor has an influence on ventricle size; we measured a volume variation $\Delta V = 4.6\ ml$ for the lateral ventricles for an initial volume of 25 ml.

To quantify the accuracy of the simulation, a medical expert manually selected corresponding feature points on the patient MRIs (see figure 14) so as to estimate these landmark displacements between March 2001 and September 2001. These measured displacements can then be compared to the ones simulated by the model. Table 4 shows the comparison results. The average displacement for selected landmarks is 2.7 mm and the corresponding average error is 1.3 mm. Without recovering the entire deformation, the proposed model captures the largest part of the displacement. The remaining error might be due to various phenomena:

- The ratio between the average deformation amplitude (2.7 mm) and the image resolution (1.0 mm) is not large enough to make accurate measurements.
- The average error (1.3 mm) is in the range of manual selection error.
- The deformation phenomenon might be larger in the sulci interstitial space than in the brain parenchyma. In this case, a finer mesh and different constitutive equations would be necessary to model the deformation.

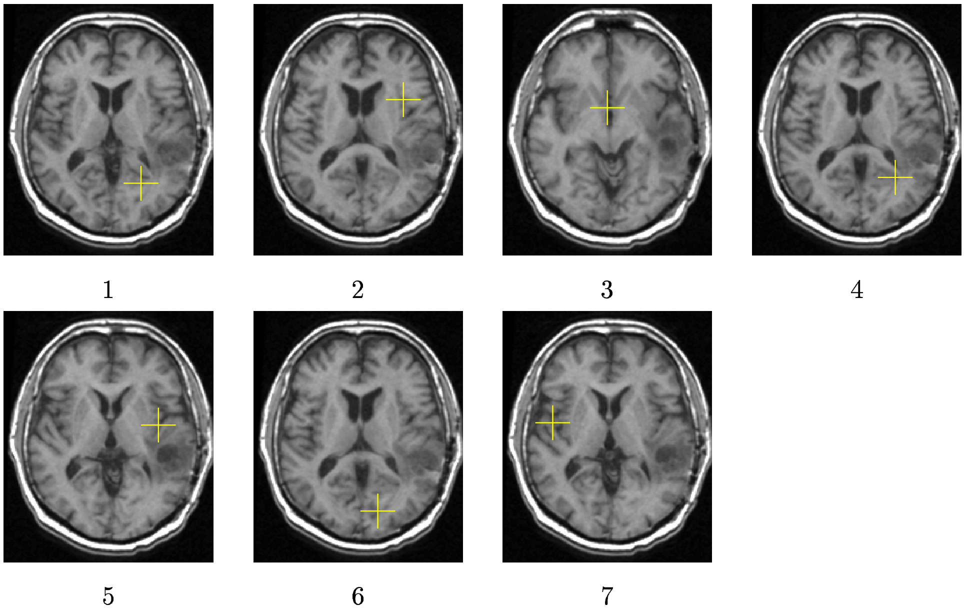

Figure 14: The 7 selected landmarks

4.1.2 Diffusion

Since we want to compare the simulation with the patient MRI, we need to establish a correspondence between the c value and the MRI gray level. However, this correspondence cannot be established in the MRI for two reasons:

Landmark #	Measured displacement [x,y,z] norm (mm)	Simulated displacement [x,y,z] norm (mm)	Error norm (mm)
1	[-3.0,1.0,1.0] 3.3	[-2.1,0.9,1.2] 2.6	0.939648
2	[-1.0,-4.0,0.0] 4.1	[-0.8,-2.3,0.8] 2.7	1.81151
3	[-1.3,-0.3,0.0] 1.3	[-1.3,-0.5,-0.1] 1.4	0.256377
4	[-3.0,0.0,-0.6] 3.0	[-2.0,0.9,1.9] 2.9	2.93169
5	[-2.3,-4.3,1.3] 5.0	[-1.7,-3.6,2.2] 4.7	1.27232
6	[-0.6,0.0,-0.3] 0.7	[-1.5,0.5,0.3] 1.6	1.15649
7	[-0.6,-1.0,-0.3] 1.2	[-0.3,-0.1,-0.2] 0.4	1.00907

Table 4: Comparison between the measured displacements and the simulated ones on selected landmarks.

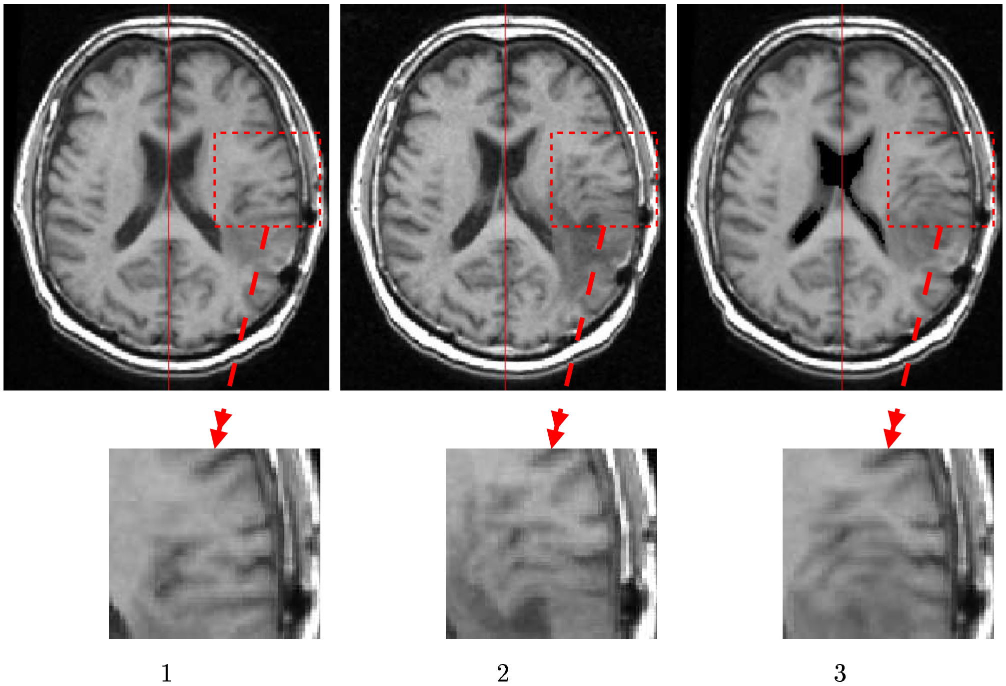

Figure 15: Visualization of the mass effect. 1. T1 MRI 03/2001, 2. T1 MRI 09/2001, 3. T1 MRI 03/2001 deformed with the simulated displacement field.

- The hyper-signal observed in the T2 MRI does not directly correspond to the tumor but to the edema.
- Unlike CT, MRI is not a calibrated measure. Thus no absolute correspondence can be made between the gray level and the nature of the tissue.

Indeed, this correspondence has been measured with CT. Tracqui et al. suggested a 8000 $cells\ mm^{-3}$ threshold of detection in [Tracqui *et al.*, 1995] for an enhanced CT scan. Figures 16, 17, 18, 19 represent a T2 MRI acquired in March 2001 (left), and the same MRI with superimposed contours interpolated between the GTV1 and the GTV2 used to initialize the tumor localization (right).

Figures 20,21,22,23, represent a T2 MRI of the same patient acquired in September 2001 (left), and the same MRI with superimposed iso-level of the predicted tumoral cells concentration above 8000 $cells\ mm^{-3}$ (right).

5 Future Work

We wish to consider two distinct areas of research for the current model. The first one consists in improving the model for simulation, the second one is related to the clinical validation and applications.

Model Improvement for Simulation

Previous results have demonstrated the ability of the numerical model to predict the tumor behavior. However, the model could be enhanced with additional characteristics:

- When diffusing into the brain parenchyma, the tumor also affects the fiber structure of the white matter. This modification of fibers structure in the invaded area could be taken into account by updating the diffusion tensor $\underline{\underline{D}}$.
- We could include more complex diffusion laws like the active cell model proposed by Tracqui [Tracqui, 1995].
- It could be interesting to consider the growth process at a cell scale and link it with the reaction-diffusion equation. The cellular automata are in this context an interesting approach to be explored.
- The model could greatly benefit from the use of more patient-specific images. More precisely, patient DTI capturing the white-matter fiber directions could greatly improve the accuracy of the simulation.
- Using alternative numerical methods like finite differences on a structured grid could lead to an increased resolution in the simulated tumor growth.

Clinical Validation and Applications

Because this article is a proof-of-concept aiming at demonstrating the feasibility of modeling complex tumors, we consider the comparison of the simulated VG with the follow-up MR image of the patient as a preliminary step toward a clinical validation. Therefore, we wish to develop other methods for the identification of parameters and for clinical validation:

- Correlation of the VG prediction with histopathological analysis of patient brains, especially in the MRI areas under the threshold of detection.
- Adding functional information to the atlas to allow the prediction of functional loss induced by the tumor growth.
- Studying the influence of the therapeutic intervention on the GBM invasion to better estimate the appropriate time for radiotherapy and surgery treatments, as proposed in [Swanson *et al.*, 2004].

We also wish to evaluate the relevance of the model on more patient datasets. This evaluation relies upon the importance of the initialization in the diffusion process, especially in the GTV2 area. Finally, we wish to investigate the possibility of extending this model to other kinds of diffusive tumors (lung, muscles).

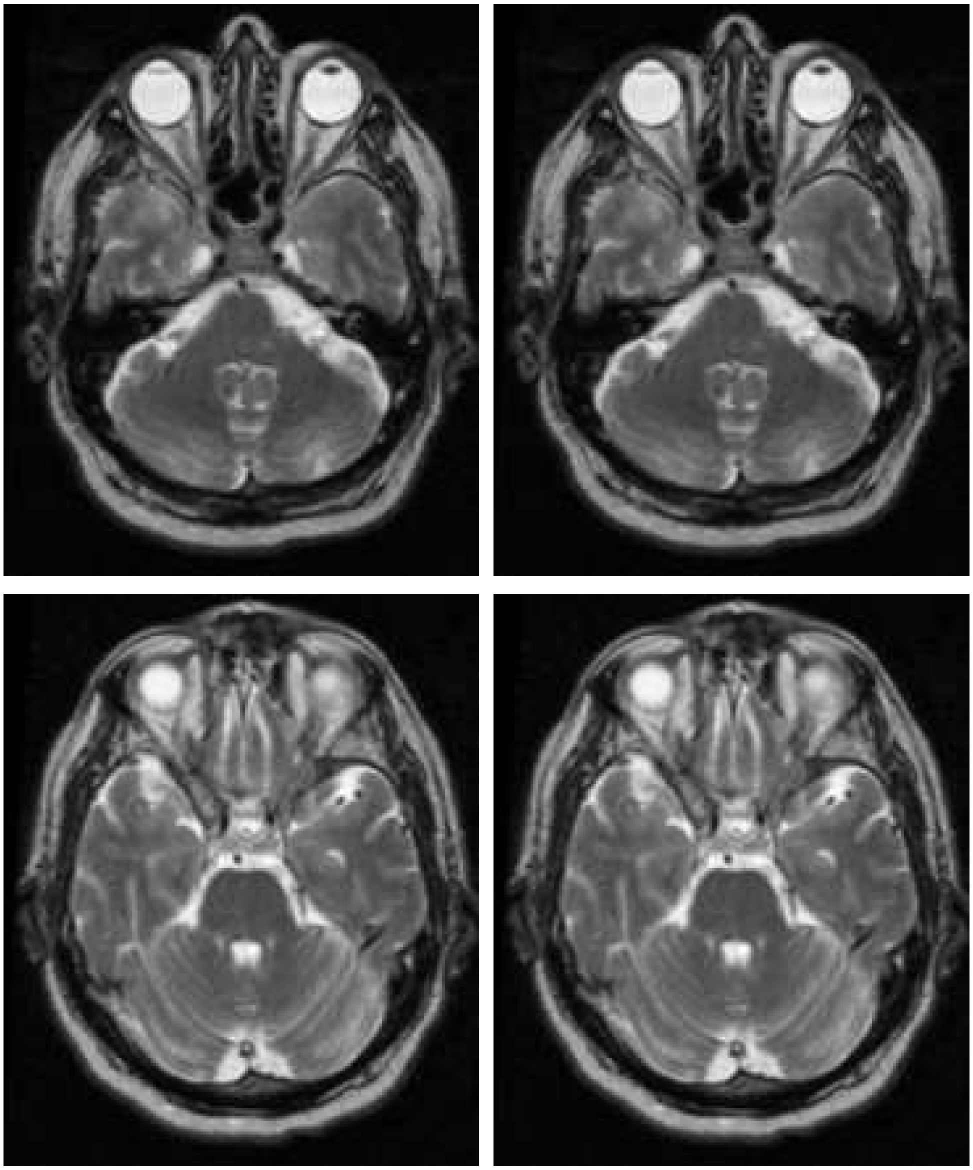

1 2

Figure 16: 1. T2 MRI 03/2001, 2. T2 MRI 03/2001 + GBM initialization

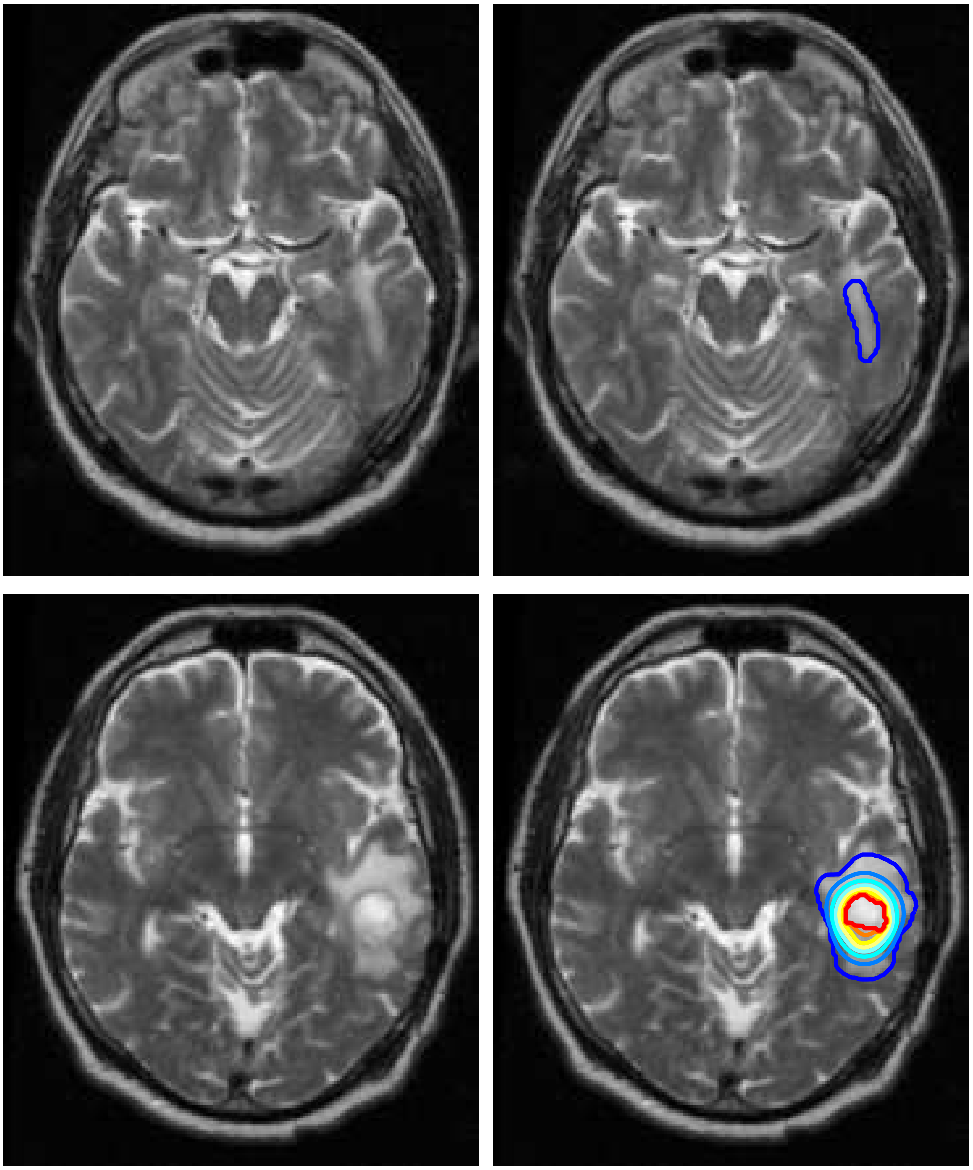

1 2

Figure 17: 1. T2 MRI 03/2001, 2. T2 MRI 03/2001 + GBM initialization

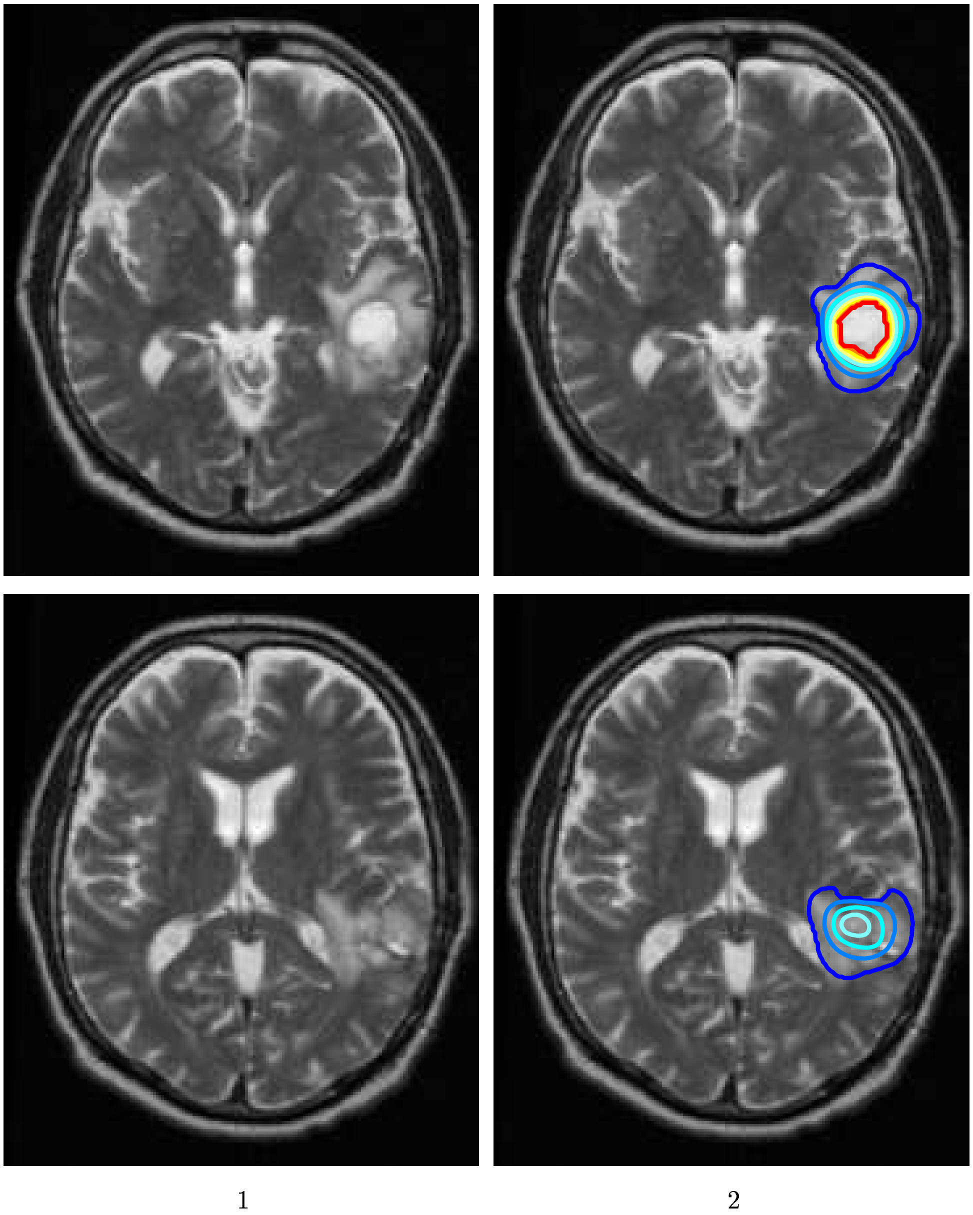

Figure 18: 1. T2 MRI 03/2001, 2. T2 MRI 03/2001 + GBM initialization

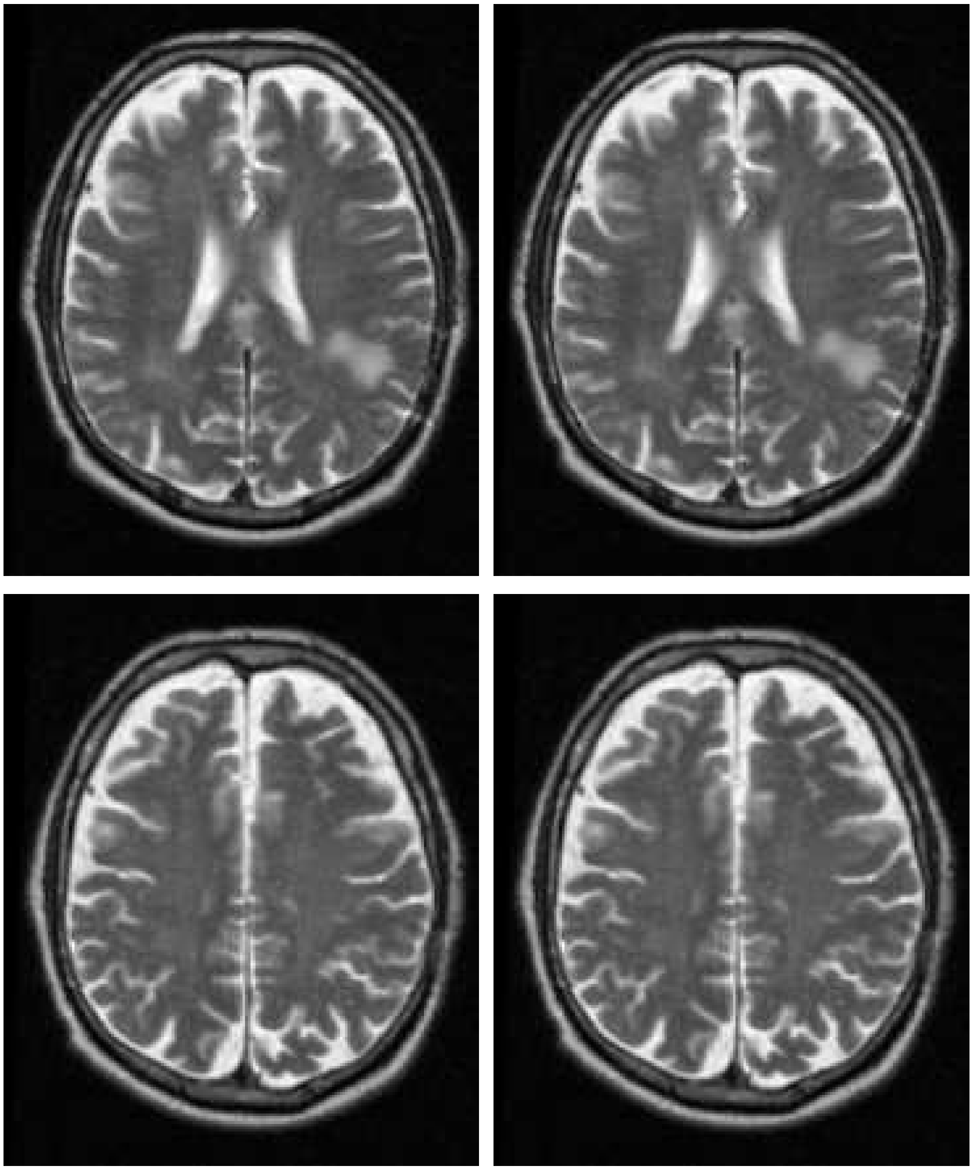

1 2

Figure 19: 1. T2 MRI 03/2001, 2. T2 MRI 03/2001 + GBM initialization

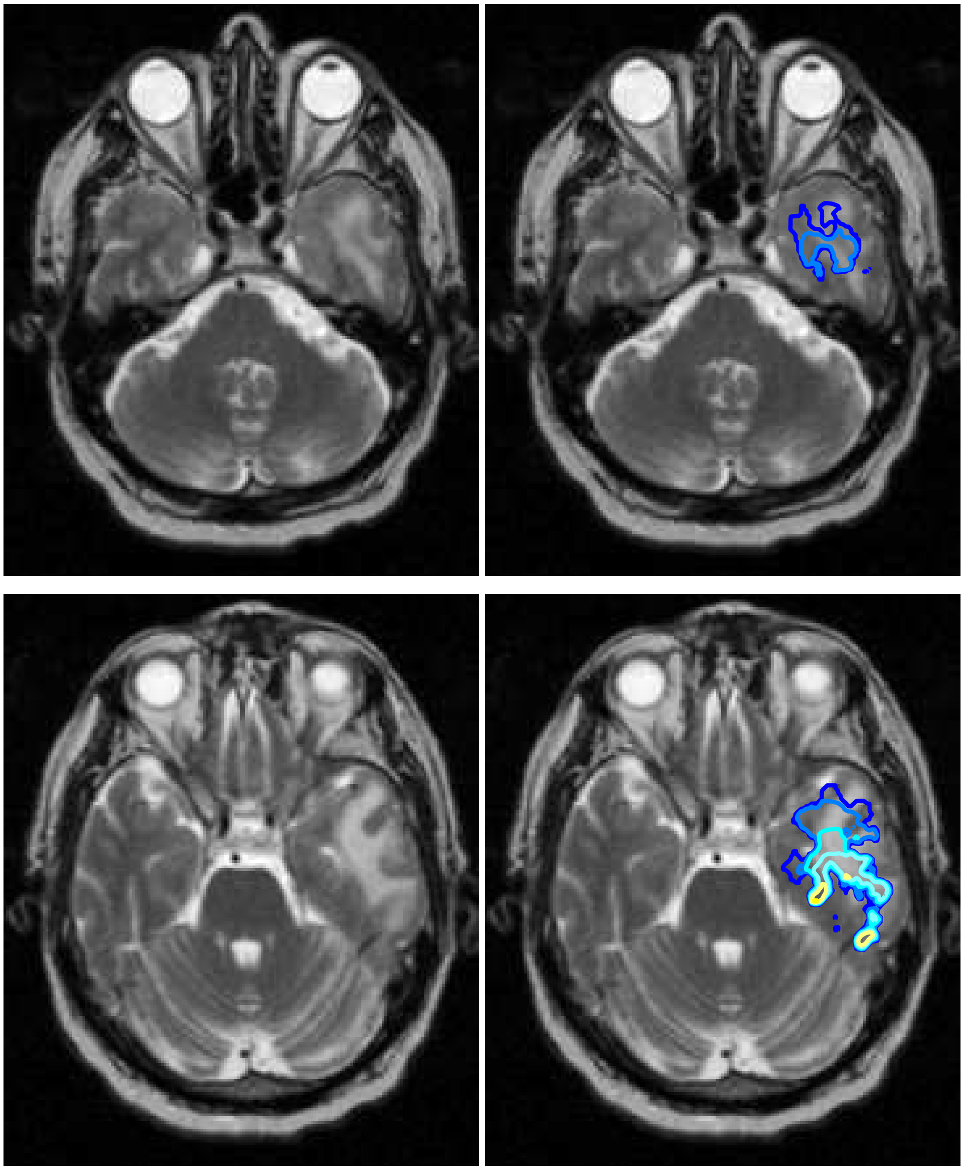

Figure 20: 1. T2 MRI 09/2001, 2. T2 MRI 09/2001 + simulated GBM

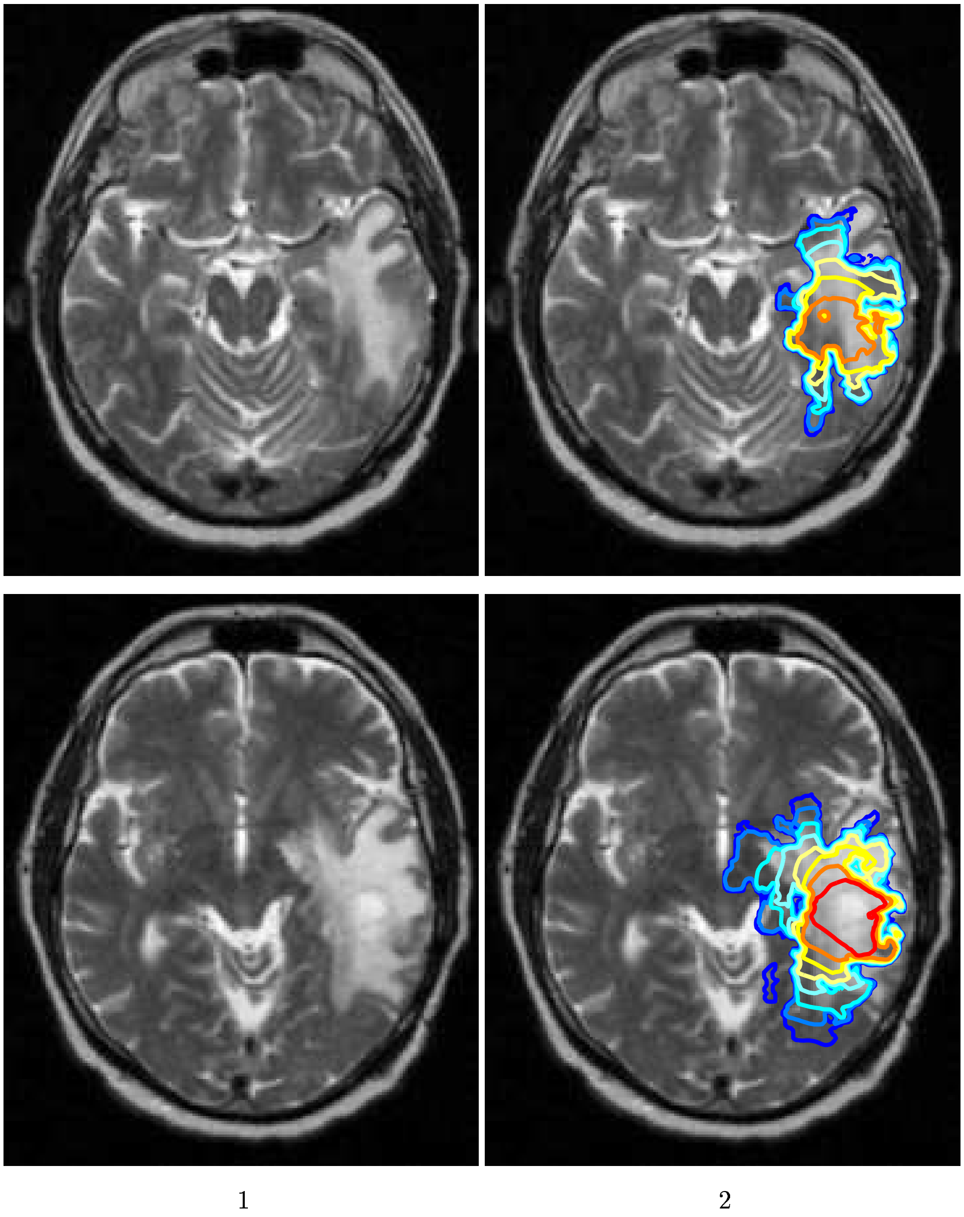

Figure 21: 1. T2 MRI 09/2001, 2. T2 MRI 09/2001 + simulated GBM

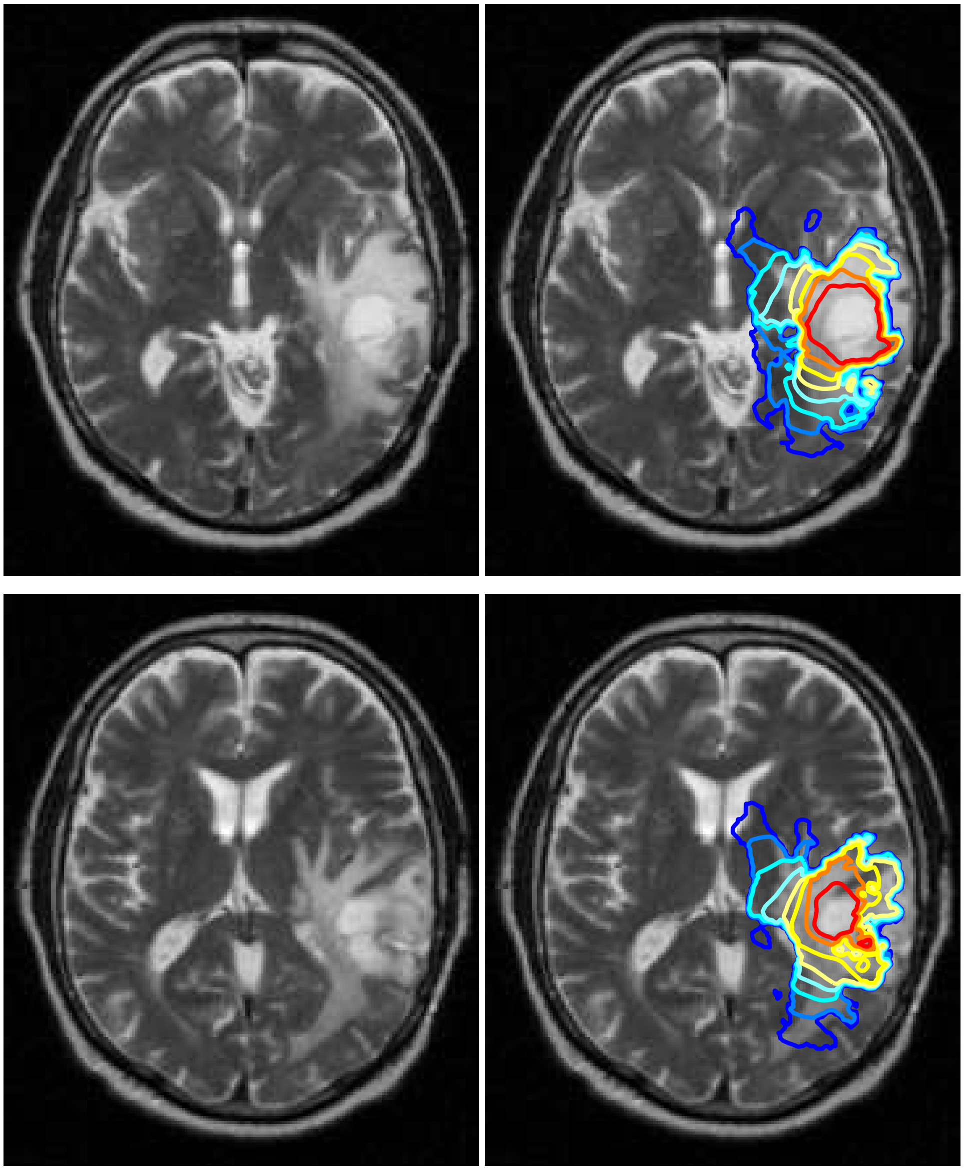

1 2

Figure 22: 1. T2 MRI 09/2001, 2. T2 MRI 09/2001 + simulated GBM

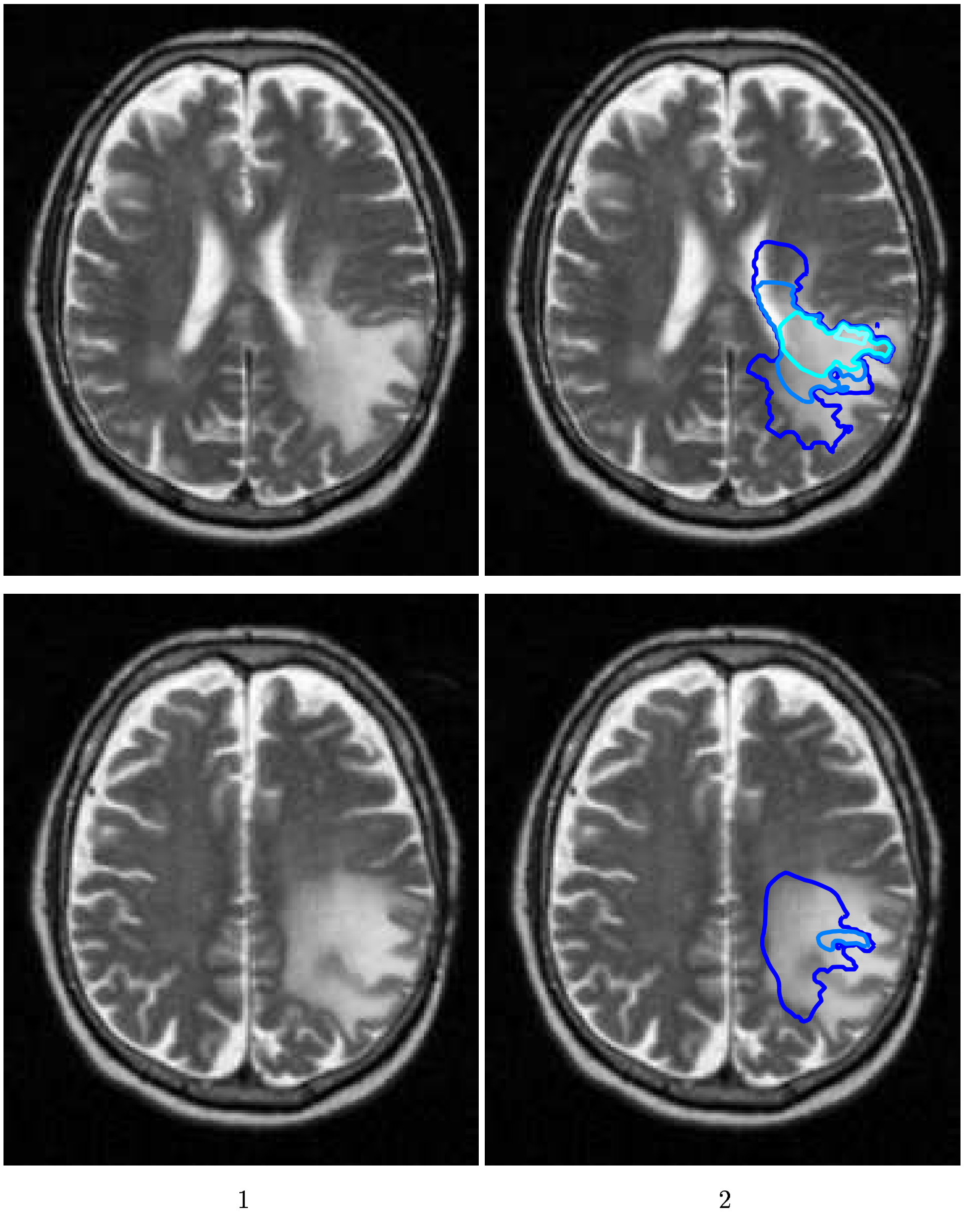

Figure 23: 1. T2 MRI 09/2001, 2. T2 MRI 09/2001 + simulated GBM

A Finite Element Modeling

Elements We use a linear tetrahedron (P_1) element to discretize our brain domain (more details about the meshing procedure can be found in the next section). Then the displacement u of any point $\underline{X}$ of the domain is defined as:

$$\underline{u}(\underline{X}) = \sum_{j=0}^{3} h_j(\underline{X})\underline{u_j} \tag{13}$$

And the cell density c:

$$c(\underline{X}) = \sum_{j=0}^{3} h_j(\underline{X})c_j \tag{14}$$

where $h_j(\underline{X})$, $j = 0, \ldots, 3$ are the shape functions that correspond to the linear interpolation inside the tetrahedron and u_j is the displacement of vertex j of the tetrahedron. Using the homogeneous coordinates, the shape functions $h_j(\underline{X})$ are related to the coordinates $\underline{P_j}$ of the tetrahedron vertices by:

$$\begin{aligned} \underline{X} &= \underline{\underline{P}}\,\underline{H} \\ \begin{bmatrix} x \\ y \\ z \\ 1 \end{bmatrix} &= \begin{bmatrix} p_0^x & p_1^x & p_2^x & p_3^x \\ p_0^y & p_1^y & p_2^y & p_3^y \\ p_0^z & p_1^z & p_2^z & p_3^z \\ 1 & 1 & 1 & 1 \end{bmatrix} \begin{bmatrix} h_0 \\ h_1 \\ h_2 \\ h_3 \end{bmatrix} \end{aligned} \tag{15}$$

The gradient $\underline{\underline{\nabla u}}(\underline{X})$ is constant inside the tetrahedron. More details about the computation of the shape function and its properties can be found in [Delingette and Ayache, 2004].

Mechanical Functional The displacement field solution of the mechanical problem is obtained by minimizing the potential energy functional E_p:

$$E_p = \frac{1}{2}\int_{\Omega} \mathrm{Tr}\left[\underline{\underline{\epsilon}}\,\underline{\underline{K}}\,\underline{\underline{\epsilon}}\right] d\Omega - \int_{\Omega} \underline{f_{ext}}\,\underline{U}\, d\Omega \tag{16}$$

Then combining equations 13 and 11 with 16 we can explicitly compute the potential energy:

$$E_p = \frac{1}{2}\,[u]^T\,[K]\,[u] - [f]^T\,[u]$$

The minimization condition can indeed be written as a linear system:

$$[K]\,[u] = [f] \tag{17}$$

Details of the matrix $[K]$ computation can be found in [Delingette and Ayache, 2004].

Diffusion Functional Searching the solution of equation 8 on a domain Ω (the brain) in a functional space $\mathcal{V}$ (here $\mathcal{V} = H^1$) is equivalent to solving:

$$\forall \psi \in \mathcal{V},\ \int_\Omega \frac{\partial c}{\partial t} \cdot \psi = \int_\Omega \left(div\left(\underline{\underline{D}}\,\underline{\nabla c}\right)\right) \cdot \psi + \int_\Omega \rho\, c \cdot \psi$$

Using the divergence theorem on the first term of the right side, and taking into account boundary conditions (details can be found in [Bathe, 1982]), yields:

$$\forall \psi \in \mathcal{V},\ \int_\Omega \frac{\partial c}{\partial t} \cdot \psi = -\int_\Omega \underline{\underline{D}}\,\underline{\nabla c} \cdot \underline{\nabla \psi} + \int_\Omega \rho\, c \cdot \psi \tag{18}$$

Then combining 14 with 18 and taking $\psi = h_j$ inside the tetrahedra, we can write the diffusion functional as:

$$\begin{aligned} \sum_{i=1}^{N} \frac{\partial c_i}{\partial t} \int_\Omega h_i h_j &= -\sum_{i=1}^{N} c_i \int_\Omega \underline{\underline{D}}\,\underline{\nabla h_i} \cdot \underline{\nabla h_j} + \sum_{i=1}^{N} [c_i] \int_\Omega \rho\, h_i h_j \\ [M]\, \frac{\partial\, [c]}{\partial t} &= (\rho\, [M] - [D])\ [c] \qquad (19) \end{aligned}$$

With the rigidity and mass matrices defined as:

$$\begin{aligned} [M] &= [M_{i,j}] = \int_\Omega h_i h_j \\ [D] &= [D_{i,j}] = \int_\Omega \underline{\underline{D}}\,\underline{\nabla h_i} \cdot \underline{\nabla h_j} \end{aligned}$$

In addition, we perform *mass lumping* which consists in concentrating the mass of tetrahedra on their vertices. The mass matrix for tetrahedron T is then defined as:

$$[M_{i,j}] = 0 \qquad [M_{i,i}] = \sum_{T/(p_i \in T)} \frac{V(T)}{4}$$

Mesh Generation The full meshing procedure can be decomposed in three steps:

- Using the atlas segmented brain, we generate a surface mesh with the fast marching cube algorithm [Lorensen and Cline, 1987].
- This surface mesh is then decimated with the YAMS (INRIA) software [Frey, 2001].
- We finally generate the volumetric mesh from the surfacic one with another INRIA software: GHS3D [Frey and George, 2000]. This software optimizes the shape quality of all tetrahedra in the final mesh

Since the structures considered in the segmentation (white fiber beams, sulci) have a small spatial size (between 1 and 4 mm), we had to use a relatively fine mesh of 250,000 tetrahedra to describe their behavior.

Tetrahedra Labeling In order to assign each tetrahedron its mechanical and diffusive properties from the five segmented classes in the atlas, we need to find the list of atlas-voxels contained in the tetrahedron. We propose to "slice" the tetrahedron, and include a voxel in a tetrahedron if its barycentric coordinates are positive. Analytically a voxel is assigned to the tetrahedron if:

$$\left\{\forall i \in [1..4]\,,\; \left[\underline{\underline{P}}^{-1}\,\underline{X}\right]_i > 0\right\}$$

The last step consists in finding the dominant class in the tetrahedron to assign it to its associated atlas class. From this class we can set the properties of the tetrahedron based on Tables 2 and 3.

B Numerical Integration

Mechanical Equation The linear system 17 can be written for each vertex i:

$$[K_{i,i}]\,[u_i] + \sum_{j\in\mathcal{N}(i)} [K_{i,j}]\,[u_j] = [f_i] \tag{20}$$

Where $\mathcal{N}(i)$ is the set of neighboring vetices of vertex i.

The principle of relaxation algorithms consists in moving each vertex in order to locally solve equation 20 (see [Saad, 1996] for details):

$$\left[{}^{+}u_i\right] = [K_{i,i}]^{-1}\,[f_i] - \sum_{j\in\mathcal{N}(i)} [K_{i,i}]^{-1}\;\; [K_{i,j}]\,[u_j] \tag{21}$$

This method does not need the computation of a global stiffness matrix inverse, and could thus be used for real-time simulation.

Diffusion Equation We propose an unconditionally stable implicit numerical scheme for the diffusion equation integration. Thus equation 19 becomes:

$$[M]\;\frac{[c]^{\tau+\Delta\tau} - [c]^{\tau}}{\Delta\tau} + [D]\;[c]^{\tau+\Delta\tau} - \rho\,[M]\;[c]^{\tau+\Delta\tau} = 0$$

Which can be written as:

$$\Big((1-\rho\Delta\tau) + [M]^{-1}\,[D]\,\Delta\tau\Big)\,[c]^{\tau+\Delta\tau} = [c]^{\tau} \tag{22}$$

In this way, we transform equation 19 into a linear system taking the form KU=F. We then use the same relaxation method for the resolution of the linear system 22 as the one proposed for the mechanical equation 20.

References

[Bajzer, 1999] Z Bajzer. Gompertzian growth as a self-similar and allometric process. *Growth Dev Aging*, 63(1-2):3–11, Spring-Summer 1999.

[Bathe, 1982] K.J. Bathe. *Finite Element Procedures in Engineering Analysis.* Prentice-Hall, Englewood Cliffs, N.J, 1982.

[Burgess *et al.*, 1997] P.K. Burgess, P.M. Kulesa, J.D. Murray, and E.C. Alvord Jr. The interaction of growth rates and diffusion coefficients in a three-dimensional mathematical model of gliomas. *Journal of Neuropathology and Experimental Neurology*, 56(6):704–713, Jun 1997.

[Bussemaker *et al.*, 1997] H. Bussemaker, A. Deutsch, and E. Geigant. Mean-field analysis of a dynamical phase transition in a cellular automaton model for collective motion. *Phys. Rev. Lett.*, 78:5018–5021, 1997.

[Chaplain, 1996] M.A.J. Chaplain. Avascular growth, angiogenesis and vascular growth in solid tumours: The mathematical modelling of the stages of tumour development. *Mathematical and Computer Modelling*, 23(6):47–88, 1996.

[Clatz *et al.*, 2003] O. Clatz, H. Delingette, E. Bardinet, D. Dormont, and N. Ayache. Patient specific biomechanical model of the brain: Application to parkinson's disease procedure. In N. Ayache and H. Delingette, editors, *International Symposium on Surgery Simulation and Soft Tissue Modeling (IS4TM'03)*, volume 2673 of *Lecture Notes in Computer Science*, pages 321–331, Juan-les-Pins, France, 2003. INRIA Sophia Antipolis, Springer-Verlag.

[Cocosco *et al.*, 1997] C.A. Cocosco, V. Kollokian, R.K.-S. Kwan, and A.C. Evans. Brainweb: Online interface to a 3d mri simulated brain database. *NeuroImage*, 5:425, 1997.

[Cruywagen *et al.*, 1995] G.C. Cruywagen, D.E. Woodward, P. Tracqui, G.T. Bartoo, J.D. Murray, and E.C. Alvord. The modelling of diffusive tumours. *Journal of Biological Systems*, 3(4):937–945, 1995.

[Delingette and Ayache, 2004] H. Delingette and N. Ayache. *Computational Models for the Human Body*, chapter Soft Tissue Modeling for Surgery Simulation. Handbook of Numerical Computing (Ed : Ph. Ciarlet). Elsevier, 2004.

[Frenay *et al.*, 2000] M Frenay, C Lebrun, M Lonjon, P Y Bondiau, and M Chatel. Up-front chemotherapy with fotemustine (f) / cisplatin (cddp) / etoposide (vp16) regimen in the treatment of 33 non-removable glioblastomas. *Eur J Cancer*, 36(8):1026–31, May 2000.

[Frey and George, 2000] Pascal Jean Frey and Paul Louis George. *Mesh Generation.* Hermes Science Publications, 8 quai du Marche neuf, 75004 Paris, May 2000.

[Frey, 2001] Pascal J. Frey. Yams a fully automatic adaptive isotropic surface remeshing procedure. Technical report RT-0252, INRIA, November 2001.

[Fung, 1993] Yuan-Cheng Fung. *Biomechanics: Mechanical Properties of Living Tissues.* Springer Verlag, January 1993.

[Haney *et al.*, 2001] S.M. Haney, P.M. Thompson, T.F. Cloughesy, J.R. Alger, and A.W. Toga. Tracking tumor growth rates in patients with malignant gliomas: A test of two algorithms. *American Journal of Neuroradiology*, 22(1):73–82, Jan 2001.

[Kansal *et al.*, 2000] A.R. Kansal, S. Torquato, E.A. Chiocca, and T.S. Deisboeck. Emergence of a subpopulation in a computational model of tumor growth. *Journal of Theoretical Biology*, 207(4):431–422, 2000.

[Kantor *et al.*, 2001] G Kantor, H Loiseau, A Vital, and J J Mazeron. [gross tumor volume (gtv) and clinical target volume (ctv) in adult gliomas]. *Cancer Radiother*, 5(5):571–80, October 2001.

[Kyriacou and Davatzikos, 2001] S.K. Kyriacou and C.A. Davatzikos. A biomechanical model of soft tissue deformation, with applications to non-rigid registration of brain images with tumor pathology. *Medical Image Computing and Computer-Assisted Intervention*, 1496:531–538, 2001.

[Laird, 1969] A K Laird. Dynamics of growth in tumors and in normal organisms. *Natl Cancer Inst Monogr*, 30:15–28, May 1969.

[Lazareff *et al.*, 1999] J A Lazareff, R Suwinski, R De Rosa, Rosa R De, and C E Olmstead. Tumor volume and growth kinetics in hypothalamic-chiasmatic pediatric low grade gliomas. *Pediatr Neurosurg*, 30(6):312–9, June 1999.

[Lorensen and Cline, 1987] W. E. Lorensen and H. E. Cline. Marching cubes: a high resolution 3d surface constructionalgorithm. In *Siggraph 87 Conference Proceedings*, volume 21 of *Computer Graphics*, pages 163–170, July 1987.

[Mayneord, 1999] W.V. Mayneord. On a law of growth of jensen's rat sarcoma. *Am.J. Cancer*, page 16:841, 1999.

[Miga *et al.*, 2000] M. I. Miga, K. D. Paulsen, F. E. Kennedy, P. J. Hoopes, A. Hartov, and D. W. Roberts. In vivo analysis of heterogeneous brain deformation computations for model-updated image guidance. *Computer Methods in Biomechanics and Biomedical Engineering*, 3(2):129–146, 2000.

[Miller, 2002] K. Miller. *Biomechanics of Brain for Computer Integrated Surgery.* Warsaw University of Technology Publishing House, 2002.

[Murray, 1989] J.D. Murray. *Mathematical Biology.* Springer-Verlag, Heidelberg, 1989.

[Ourselin *et al.*, 2000] S. Ourselin, A. Roche, S. Prima, and N. Ayache. Block Matching: A General Framework to Improve Robustness of Rigid Registration of Medical Images. In A.M. DiGioia and S. Delp, editors, *Third International Conference on Medical Robotics, Imaging And Computer Assisted Surgery (MICCAI 2000)*, volume 1935 of *Lectures Notes in Computer Science*, pages 557–566, Pittsburgh, Pennsylvanie USA, octobre 11-14 2000. Springer.

[Patel *et al.*, 2001] A.A. Patel, E.T. Gawlinski, S.K. Lemieux, and R.A. Gatenby. A cellular automaton model of early tumor growth and invasion. *Journal of Theoretical Biology*, 213(3):315–331, Dec 2001.

[Price *et al.*, 2003] S.J. Price, N.G. Burnet, T. Donovan, H.A. Green, A. Pena, N.M. Antoun, J.D. Pickard, T.A. Carpenter, and J.H. Gillard. Diffusion tensor imaging of brain tumours at 3t: A potential tool for assessing white matter tract invasion ? *Clin Radiol*, 58(6):455–462, June 2003.

[Retsky *et al.*, 1990] M W Retsky, D E Swartzendruber, R H Wardwell, and P D Bame. Is gompertzian or exponential kinetics a valid description of individual human cancer growth? *Med Hypotheses*, 33(2):95–106, October 1990.

[Rousseeuw, 1984] P. Rousseeuw. Least median-of-squares regression. *Journal of the American Statistical Association*, 79, 1984.

[Saad, 1996] Yousef Saad. *Iterative Methods for Sparse Linear Systems.* PWS Publishing, Boston, MA, 1996.

[Schill *et al.*, 1996] M. Schill, M. Schinkmann, H.-J. Bender, and R. Männer. Biomechanical simulation of the falx cerebri using the finite element method. In *18. Annual International Conference, IEEE Engeneering in Medicine and Biology. S*, 1996.

[Sierra, 2001] Raimundo Sierra. Nonrigid registration of diffusion tensor images. Master's thesis, Swiss Federal Institute of Technology Zurich, 2001.

[Stevens, 2000] S.A. Stevens. Mean pressures and flows in the human intracranial system, determined by mathematical simulations of a steady-state infusion test. *Neurological Research*, 22:809–814, 2000.

[Swanson *et al.*, 2000] K.R. Swanson, E.C. Alvord Jr, and J.D. Murray. A quantitative model for differential motility of gliomas in grey and white matter. *Cell Proliferation*, 33(5):317–329, Oct 2000.

[Swanson *et al.*, 2002] K.R. Swanson, E.C. Alvord Jr, and J.D. Murray. Virtual brain tumours (gliomas) enhance the reality of medical imaging and highlight inadequacies of current therapy. *British Journal of Cancer*, 86(1):14–18, Jan 2002.

[Swanson *et al.*, 2003] K.R. Swanson, Carly Bridge, J D Murray, and Ellsworth C Alvord. Virtual and real brain tumors: using mathematical modeling to quantify glioma growth and invasion. *J Neurol Sci*, 216(1):1–10, Dec 2003.

[Swanson *et al.*, 2004] K. R. Swanson, E. C. Alvord Jr., and J. D. Murray. Dynamics of a model for brain tumors reveals a small window for therapeutic intervention. *Discrete and Continuous Dynamical Systems*, 4(1):289–285, 2004.

[Talairach and Tournoux, 1988] Jean Talairach and Pierre Tournoux. *Co-Planar Stereotaxic Atlas of the Human Brain: 3-Dimensional Proportional System: An Approach to Cerebral Imaging.* Thieme Medical Pub, October 1988.

[Tracqui and Mendjeli, 1999] Philippe Tracqui and Mahidine Mendjeli. Modelling three-dimensional growth of brain tumours from time series of scans. *Mathematical Models and Methods in Applied Sciences*, 19(4):581–598, June 1999.

[Tracqui *et al.*, 1995] P. Tracqui, G.C. Cruywagen, D.E. Woodward, G.T. Bartoo, J.D. Murray, and E.C. Alvord Jr. A mathematical model of glioma growth: the effect of chemotherapy on spatio-temporal growth. *Cell Proliferation*, 28(1):17–31, Jan 1995.

[Tracqui, 1995] P. Tracqui. From passive diffusion to active cellular migration in mathematical models of tumour invasion. *Acta Biotheoretica*, 43(4):443–464, Dec 1995.

[Wasserman and Acharya, 1996] R. Wasserman and R. Acharya. A patient-specific in vivo tumor model. *Mathematical Biosciences*, 136(2):111–140, Sep 1996.

Unité de recherche INRIA Sophia Antipolis
2004, route des Lucioles - BP 93 - 06902 Sophia Antipolis Cedex (France)

Unité de recherche INRIA Futurs : Parc Club Orsay Université - ZAC des Vignes
4, rue Jacques Monod - 91893 ORSAY Cedex (France)
Unité de recherche INRIA Lorraine : LORIA, Technopôle de Nancy-Brabois - Campus scientifique
615, rue du Jardin Botanique - BP 101 - 54602 Villers-lès-Nancy Cedex (France)
Unité de recherche INRIA Rennes : IRISA, Campus universitaire de Beaulieu - 35042 Rennes Cedex (France)
Unité de recherche INRIA Rhône-Alpes : 655, avenue de l'Europe - 38334 Montbonnot Saint-Ismier (France)
Unité de recherche INRIA Rocquencourt : Domaine de Voluceau - Rocquencourt - BP 105 - 78153 Le Chesnay Cedex (France)

Éditeur
INRIA - Domaine de Voluceau - Rocquencourt, BP 105 - 78153 Le Chesnay Cedex (France)
http://www.inria.fr
ISSN 0249-6399